HHS Public Access

Author manuscript

Nat Aging. Author manuscript; available in PMC 2024 June 27.

Published in final edited form as:

Nat Aging. 2023 November ; 3(11): 1387–1400. doi:10.1038/s43587-023-00505-y.

TET2 modulates spatial relocalization of heterochromatin in aged hematopoietic stem and progenitor cells

Tingting Hong[1,8], **Jia Li**[1,7,8], **Lei Guo**[1], **Maryn Cavalier**[1], **Tianlu Wang**[1], **Yaling Dou**[1], **Aaron DeLaFuente**[1], **Shaohai Fang**[1], **Anna Guzman**[2,3], **Katherina Wohlan**[2,3], **Chiraag Kapadia**[2,3], **Carina Rosas**[2,3], **Yaling Yang**[4], **C. Cameron Yin**[4], **Shaoying Li**[4], **M. James You**[4], **Xiaodong Cheng**[5], **Margaret A. Goodell**[2,3], **Yubin Zhou**[1,6], **Yun Huang**[1,6]

[1]Institute of Biosciences and Technology, Texas A&M University, Houston, TX, USA.

[2]Department of Molecular Cell Biology, Baylor College of Medicine, Houston, TX, USA.

[3]Stem Cells and Regenerative Medicine Center, Baylor College of Medicine, Houston, TX, USA.

[4]Department of Leukemia, The University of Texas MD Anderson Cancer Center, Houston, TX, USA.

[5]Department of Epigenetics and Molecular Carcinogenesis, The University of Texas MD Anderson Cancer Center, Houston, TX, USA.

[6]Department of Translational Medical Sciences, School of Medicine, Texas A&M University, Houston, TX, USA.

[7]Present address: State Key Laboratory of Respiratory Disease, First Affiliated Hospital of Guangzhou Medical University, Guangzhou, Guangdong, China.

[8]These authors contributed equally: Tingting Hong, Jia Li.

Abstract

DNA methylation deregulation at partially methylated domains (PMDs) represents an epigenetic signature of aging and cancer, yet the underlying molecular basis and resulting biological

Correspondence and requests for materials should be addressed to Jia Li, Yubin Zhou or Yun Huang., jiali@tamu.edu; yubinzhou@tamu.edu; yun.huang@tamu.edu.

Author contributions

Y.H. and Y.Z. directed and supervised the project. T.H. performed most animal-related work, molecular characterization and sequencing library preparation. J.L. performed all the bioinformatics analysis on high-throughput sequencing data. L.G., T.W. and S.F. supported sequencing library preparation. Y.D. performed cell sorting. A.D. and M.C. performed genotyping and supported molecular cloning. A.G., K.W., C.R. and C.K. supported animal-related work. Y.Y., C.C.Y., S.L. and M.J.Y. provided human bone marrow samples. M.A.G. and X.C. provided essential resources and key intellectual inputs to support this study. Y.H. and Y.Z. wrote the paper. All the authors participated in the discussion, data interpretation and paper editing or discussion.

Additional information

Extended data is available for this paper at https://doi.org/10.1038/s43587-023-00505-y.

Supplementary information The online version contains supplementary material available at https://doi.org/10.1038/s43587-023-00505-y.

Peer review information *Nature Aging* thanks Gerald de Haan, Francesco Neri, and Karl Lenhard Rudolph for their contribution to the peer review of this work.

Competing interests

The authors declare no competing interests.

consequences remain unresolved. We report herein a mechanistic link between disrupted DNA methylation at PMDs and the spatial relocalization of H3K9me3-marked heterochromatin in aged hematopoietic stem and progenitor cells (HSPCs) or those with impaired DNA methylation. We uncover that TET2 modulates the spatial redistribution of H3K9me3-marked heterochromatin to mediate the upregulation of endogenous retroviruses (ERVs) and interferon-stimulated genes (ISGs), hence contributing to functional decline of aged HSPCs. TET2-deficient HSPCs retain perinuclear distribution of heterochromatin and exhibit age-related clonal expansion. Reverse transcriptase inhibitors suppress ERVs and ISGs expression, thereby restoring age-related defects in aged HSPCs. Collectively, our findings deepen the understanding of the functional interplay between DNA methylation and histone modifications, which is vital for maintaining heterochromatin function and safeguarding genome stability in stem cells.

Epigenetic deregulation is a hallmark feature commonly observed in pathological conditions such as aging and cancer[1,2]. DNA methylation drifting and increased DNA methylation variation at heterochromatin are commonly observed in aged cells and malignant cells[3–5]. These regions, termed partially methylated domains (PMDs), possess several key attributes: they are lamina associated, enriched with H3K9me3, late replicated and classified within the B compartment in HiC analysis[4,6,7]. Despite often being considered as gene-less regions, heterochromatin constitutes a major component in the eukaryotic nucleus to maintain genome stability[8–10]. Although the positive correlation between DNA methylation and H3K9me3-marked heterochromatin has been long noted, two pressing questions remain unresolved. Does deregulation of DNA methylation at PMDs lead to heterochromatin dysfunction? What are the specific biological consequences stemming from this deregulation at PMDs?

The balance of DNA methylation and demethylation (abbreviated as (de)methylation hereafter) hinges on two primary families of epigenetic enzymes: the DNA methyltransferases (DNMT1–DNMT3) and the Ten-eleven translocation family of dioxygenases (TET1–TET3)[11–14]. Notably, mutations in *DNMT3A* and *TET2* are prevalent in aged individuals with clonal hematopoiesis (CH) and in those diagnosed with hematological malignancies[15–17]. DNMTs drive the production of 5-methylcytosine (5mC), whereas TET enzymes oxidize 5mC to yield 5-hydroxymethylcytosine (5hmC as the major product) and further oxidized species to facilitate DNA demethylation. In general, 5mC is highly deposited within heterochromatin (or B-compartment in HiC analysis) and maintains heterochromatin stability[18–20]. By contrast, TETs and 5hmC tend to reside in euchromatin regions (or A-compartment) and play important roles in maintaining chromatin accessibility[20–22]. This dichotomy has been recently challenged because of the observation of DNMTs redistribution from heterochromatin to euchromatin in TET-deficient cells, suggesting a yet-to-be-explained interplay between DNMT and TET proteins that intricately regulates genomic DNA (de) methylation balance at both heterochromatin and euchromatin[20]. To date, experimental evidence to substantiate the DNMT-TET interplay across heterochromatin and euchromatin in physiologically relevant contexts remains rather sparse. Furthermore, the implications of DNA (de)methylation deregulation, along with the concomitant changes in genomic distribution of DNMT and TET, on gene transcription and cellular functionality remain unclear.

In this Article, we discover that aged hematopoietic stem and progenitor cells (HSPCs) show DNA methylation loss at heterochromatin regions marked by H3K9me3. These H3K9me3-marked genomic regions undergo spatial redistribution within the nuclei of HSPCs with defective DNA methylation, as seen in aged HSPCs or those with Dnmt loss-of-function (LOF). Tet2 appears to be the primary mediator of this process, which contributes to augmented transcription of endogenous retrovirus (ERVs) and interferon-stimulated genes (ISGs), potentially influencing the functional decline of aged HSPCs. These findings underscore the coordinated roles of DNMT and TET in preserving DNA methylation balance in both heterochromatin and euchromatin throughout HSPCs aging. Our study also lends key insights into the mechanisms underlying aging-related heterochromatin dysfunction at PMDs that contributes to the functional deterioration of aged HSPCs.

Results

Tet2 depletion counteracts functional decline in aged HSPCs

To evaluate the impact of aging on the self-renewal capability of HSPCs (marked by lineage-negative, Sca1$^+$, cKit$^+$; LSK) in wild-type (WT) and *Tet2*-knockout *(Tet2*KO) mice, we performed in vitro serial colony-forming unit (CFU) assay and in vivo bone marrow transplantation (BMT) experiments (Fig. 1a and Extended Data Fig. 1a). In aged WT HSPCs (18–24 months old), self-renewal and repopulation capabilities were diminished compared to the WT-young (6–8 weeks old) group. However, Tet2 depletion in HSPCs effectively rescued this age-related functional decline (Fig. 1b–d, Extended Data Fig. 1b–e, Supplementary Table 1 and Supplementary Information). In the BMT experiment, WT-old donor cells exhibited an increased myeloid cell population and a reduction in the B cell repopulation capability compared to WT-young donor cells (Fig. 1c, Extended Data Fig. 1d and Supplementary Table 1). A similar trend was observed in recipient mice receiving *Tet2*KO-young or *Tet2*KO-old cells, albeit less pronounced. At 12 weeks after BMT for both the WT and *Tet2*KO groups, we observed a higher fraction of long-term hematopoietic stem cells (LT-HSC; LSK CD150$^+$ CD48$^-$) and a lower fraction of multipotent progenitors (MPPs; defined as LSK CD150$^-$ CD48$^+$) within the LSK population in recipient mice with aged donor cells compared to those receiving young donor cells (Fig. 1d and Extended Data Fig. 1e). Recipient mice with *Tet2*KO donor cells showed a prominent increase in the ST-HSC fraction compared to those with WT donor cells (Fig. 1d and Extended Data Fig. 1e). This finding might explain the elevated repopulation efficiency of *Tet2*KO HSPCs, given that the short-term HSC (ST-HSC; defined as LSK CD150$^-$ CD48$^-$) is recognized as a major source for hematopoietic stem cell maintenance in mice[23]. Secondary BMT experiments ruled out the possibility of malignant transformation in aged HSPCs when using aged *Tet2*KO HSPCs as donor cells (Extended Data Fig. 1f,g).

Next, to determine whether aged *Tet2*KO HSPCs have a greater clonal expansion advantage than WT HSPCs, potentially accounting for age-related clonal expansion, we performed competition experiments by mixing WT HSPCs (CD45.2$^+$) with *Tet2*KO (CD45.1$^+$CD45.2$^+$) HSPCs from either young or old mice at a 9:1 ratio. We then proceeded with the same CFU and BMT experiments described above (Fig. 1e). Although *Tet2*KO HSPCs outcompeted WT HSPCs under both young and old conditions, *Tet2*KO-old HSPCs

mixed with WT-old HSPCs displayed a markedly enhanced competitive capacity compared to the young mixed group (Fig. 1f–h, Extended Data Fig. 1h and Supplementary Table 1). Post-BMT experiment lineage analysis underscored a notable repopulation advantage of *Tet2*KO-old HSPCs over *Tet2*KO-young cells across both lymphoid and myeloid lineages (red versus blue curves; Fig. 1h). Collectively, data from both ex vivo and in vivo assessments suggest that Tet2 depletion can counteract functional decline by retaining strong self-renewal and repopulation potential in HSPCs during aging.

Aged *Tet2*KO HSPCs show fewer transcriptional changes than WT HSPCs

To systematically portrait the transcriptomic landscapes of HSPCs during aging, we isolated Lin^- cells from congenic WT and *Tet2*KO (young or old) mice without prior BMT and performed single-cell RNA-seq (scRNA-seq) analysis (Fig. 2a, Extended Data Fig. 2a,b and Supplementary Table 2). Among 26,316 analyzed cells, we identified 15 clusters that represent various progenitors or lineages during hematopoiesis (Fig. 2a, Extended Data Fig. 2a,b and Supplementary Table 2). For data quality assurance, we compared the transcriptomes of our samples with previously published scRNA-seq data using young HSPCs from WT and *Tet2*KO mice[24], observing substantial consistency between datasets (Extended Data Fig. 2c and Supplementary Information). Our results highlighted distinct cell distribution within each cluster among the four experimental groups: WT-young, WT-old, *Tet2*KO-young and *Tet2*KO-old (Fig. 2b,c). Both the WT-old and *Tet2*KO-old groups displayed an elevated HSC fraction (Fig. 2c). This observation was independently corroborated by flow cytometry analysis on HSPCs from congenic WT and *Tet2*KO (young versus old) mice (Fig. 2d). Echoing results from the BMT study (Fig. 1d), LSK as a fraction of the lineage-negative population was notably higher in both the WT-old and *Tet2*KO-old groups (Fig. 2d). Among LSK cells, the percentage of LT-HSC was significantly increased in both WT-old and *Tet2*KO-old mice. In contrast, aging led to a slight decrease in the MPP fraction (Fig. 2d). Aging seemed to impose minor effects on ST-HSCs in WT mice, whereas *Tet2*KO mice displayed a pronounced increase in the ST-HSC fraction as they aged (Fig. 2d). For both the WT and *Tet2*KO groups, scRNA-seq analysis revealed a decrease in the erythroid progenitor fraction but an increase in the myeloid progenitor population during aging (Fig. 2c), which dovetailed with previous findings[25–29]. Upon Tet2 depletion, myeloid bias was prominently observed even at a young age and remained strong throughout the aging process (Fig. 2c). This observation was reinforced by flow cytometry analysis on bone marrow samples from WT-young, WT-old, *Tet2*KO-young and *Tet2*KO-old mice (Extended Data Fig. 2d,e).

A higher fraction of HSC was detected in both WT-old and *Tet2*KO-old groups compared to their younger equivalents, dovetailing with the flow cytometry analysis results (Fig. 2c,d and Supplementary Information). Given that *Tet2*KO-old HSCs retained robust self-renewal and repopulation abilities whereas WT-old HSCs showed clear functional decline (Fig. 1), we posited that these two old HSC groups might possess distinct molecular features that mirror their functional disparities. We therefore concentrated our subsequent analysis on the HSC fraction identified by scRNA-seq analysis (Fig. 2e). Because cell cycle-related genes often manifest transcriptional variations in HSCs and are typically influenced by aging[30], we performed additional analysis on these genes as previously reported[30,31] (left panel, Fig.

2e; and Extended Data Fig. 2f). According to the expression of cell cycle-related genes at the G0, G1/S and G2/M stages, HSCs could be separated into three distinct clusters. Concurrently, we performed a pseudotime analysis[32] on these cell cycle-related genes (right panel, Fig. 2e, and Extended Data Fig. 2g). We observed a higher G0 (non-cycling or quiescent) population in WT-old HSCs compared to the WT-young HSCs. In contrast, the *Tet2*KO group showed less changes in the G0 population between their young and old HSC subsets (Fig. 2g). To further corroborate these findings, we treated four groups of mice with 5-ethynyl-2′-deoxyuridine (EdU) for 24 h and assessed EdU uptake in the LT-HSC fraction (Fig. 2h). In line with a previous study[31], we found a marked decrease in the EdU signal for LT-HSCs obtained from WT-old mice compared to the WT-young group. This reduction was absent in the *Tet2*KO-aged group. Together, these findings imply that, although the HSC fraction remains high in both WT-old and *Tet2*KO-old mice, *Tet2*KO-old HSCs seem to maintain efficient cell cycle progression during aging.

In parallel, we performed bulk RNA-seq on LSK cells purified from WT-young, WT-old, *Tet2*KO-young and *Tet2*KO-old mice. We identified a total of 1,348 genes that showed prominent changes as WT HSPCs aged, which we termed age-related differentially expressed genes (DEGs) (Supplementary Table 3). Assessing these DEGs under the *Tet2*KO condition, we noticed much less difference between *Tet2*KO-young and *Tet2*KO-old HSPCs (Fig. 2i). Gene set enrichment analysis indicated that these age-related DEGs were primary involved in immune response (upregulated genes) and hematopoiesis (down-regulated genes) (Fig. 2j). We further validated the expression of selected DEGs involved in immune response (for example, *Ccl5, Cxcl10, Irf7, Oas3* and *Isg15*) by real-time quantitative PCR (qPCR) (Fig. 2k). Again, we observed significant upregulation of these genes in the WT groups (young versus old), but not in the *Tet2*KO groups. Collectively, these data confirm that substantial changes in transcriptional outputs occur when WT HSPCs age, whereas *Tet2*KO HSPCs undergo fewer transcriptional alterations during the aging process.

Tet2 depletion prevents heterochromatin relocalization

We next evaluated 5hmC levels, a major catalytic product of Tet2 (ref. 13), in HSPCs obtained from WT-young, WT-old, *Tet2*KO-young and *Tet2*KO-old mice. No obvious global changes were noted in 5hmC and *Tet2* expression between young and old WT HSPCs (Fig. 3a,b and Extended Data Fig. 3a). We further moved on to perform genome-wide cytosine-5-methylene sulfonate followed by immunoprecipitation and sequencing (CMS-IP-seq)[33,34], anticipating identifying genomic regions that might exhibit loci-specific 5hmC alterations during aging. Indeed, we identified 3,114 and 5,450 differentially hydroxymethylated regions (DHMRs) between young and old HSPCs in both WT and *Tet2*KO groups (Supplementary Table 4), respectively. However, the genomic distribution and annotated functions of these age-related DHMRs remained similar between WT and *Tet2*KO HSPCs (Extended Data Fig. 3c,d), which cannot explain the differential aging process observed between the two groups. Because age-related DNA methylation loss often occurs at heterochromatin[4], we next evaluated 5hmC changes within heterochromatin. We first performed H3K9me3 ChIP-seq to identify the heterochromatin regions in HSPCs[9]. We found that 5hmC was enriched within H3K9me3-depleted euchromatins, consistent with earlier findings[20,21] (Fig. 3c and Extended Data Fig. 3e). Interestingly, we noted a

significant rise in 5hmC within H3K9me3-marked heterochromatin in aged WT HSPCs compared to their young counterparts, whereas this trend was less pronounced in *Tet2*KO HSPCs (Fig. 3d,e).

To further assess the impact of 5hmC alterations within H3K9me3-marked heterochromatin in aged HSPCs, we performed immunofluorescence (IF) staining and immunoblotting analysis on H3K9me3. Interestingly, we observed distinct subnuclear distribution patterns for H3K9me3-marked regions: nuclear periphery (WT-young) versus nucleoplasm (WT-old) in WT HSPCs. By comparison, aging had no apparent effects on the subnuclear distribution of H3K9me3-positive regions in *Tet2*KO HSPCs (Fig. 3f,g and Extended Data Fig. 4a). Notably, the nuclear periphery-to-nucleoplasm redistribution was solely evident in H3K9me3-positive regions, contrasting regions marked by H3K9me2, a histone mark that is reported to favor localization at the nuclear periphery[35] (Fig. 3f,g and Extended Data Fig. 4a). The protein levels of H3K9me2 and H3K9me3 remained largely the same among the four experimental groups (Extended Data Fig. 4b). Similar nuclear distribution patterns of H3K9me3-positive regions were also observed in human bone marrow $CD34^+$ cells at different ages (Extended Data Fig. 4c). IF staining and immunoblotting analysis of other major histone marks (including H3K4me3, H3K27ac and H3K27me3) and lamin B1 remain largely unaltered between young and old HSPCs (Extended Data Fig. 4b,d), suggesting that age-related subnuclear change is specific to H3K9me3-positive regions.

Subsequently, we performed H3K9me3 ChIP-seq in HSPCs to map its genomic binding profile, using H3K9me2 as the mark for genomic regions located at the nuclear periphery. The overall distribution of H3K9me2 and H3K9me3 remained the same across the four analyzed groups (Fig. 3h,i and Extended Data Fig. 3b), suggesting that the altered H3K9me3 distribution in aged WT HSPC stems from the spatial relocalization of H3K9me3-marked heterochromatin rather than changes in genomic binding of H3K9me3 (Fig. 3j).

DNA methylation loss is tied to heterochromatin dysfunction

5mC is known to be enriched at H3K9me3-marked heterochromatin and plays an essential role in regulating heterochromatin stability[8]. We therefore analyzed the DNA methylation landscapes in HSPCs by using whole-genome bisulfite sequencing (WGBS). Both WT and *Tet2*KO HSPCs showed a global reduction in DNA methylation during aging (Fig. 4a,b and Extended Data Fig. 5a,b), suggesting that Tet2 only partially contributes to the age-related global DNA methylation loss. Similar observation was also reported in naïve hypomethylated embryonic stem cells[36]. Next, we sought to identify age-related differentially methylated regions (DMRs) between young and old HSPCs from WT (n = 5,925) and *Tet2*KO (n = 2,403) mice (Supplementary Table 5). Age-related DMRs identified from WT HSPCs were largely consistent with published datasets[2] (Extended Data Fig. 5c,d and Supplementary Table 5). GREAT analysis suggested that these DMRs were tied to genes involved in immune response and hematopoietic organ development (Supplementary Table 5). Given the aforementioned spatial relocalization of H3K9me3-positive regions in aged HSPCs, we focused on evaluating DNA methylation within H3K9me3-marked genomic regions. By comparing DNA methylation changes at each CpG site between young and old HSPCs, we detected remarkable DNA methylation variations during aging (Fig.

4b,c and Extended Data Fig. 5e). This aging-related DNA methylation variation was more prominently observed in H3K9me3-marked heterochromatin than in euchromatin (Fig. 4b,c and Extended Data Fig. 5e), dovetailing with increased DNA methylation variation within the PMDs observed in aged cells[4,5].

Based on these findings, we postulate that DNA methylation deregulation at heterochromatin (for example, Dnmt loss-of-function) could enable Tet2-mediated spatial relocalization of H3K9me3-positive regions (Fig. 4d). To explore this, we used a MxCre-*Dnmt3a*f/f mice model[37], in which acute depletion of de novo DNMT via polyinosinic-polycytidylic acid (pIpC) treatment could disrupt DNA methylation homeostasis within a short time window to avoid potential secondary compensatory effects. Of note, *DNMT3A* is frequently mutated in hematological malignancies[15] and the MxCre-*Dnmt3a*f/f transgenic line is regarded as a disease-relevant model to study DNA methylation. We purified HSPCs from MxCre and MxCre-*Dnmt3a*f/f mice[37], with the animals subjected to pIpC treatment at 6 weeks old and HSPCs analyzed at 10 weeks old (Extended Data Fig. 5f). We then carried out genome-wide 5mC and 5hmC profiling using WGBS and CMS-IP-seq, respectively. We observed genome-wide DNA methylation loss in *Dnmt3a*-KO HSPCs (Extended Data Fig. 5g). By comparing DNA methylation changes between *Dnmt3a*-KO and control HSPCs, we noticed a higher DNA methylation variation in heterochromatin than in euchromatin upon Dnmt3a depletion (Fig. 4b,c and Extended Data Fig. 5e). Concurrently, we observed an increase of 5hmC deposition within H3K9me3-marked heterochromatin, but not in euchromatin, following Dnmt3a depletion (Fig. 4e,f). These findings suggest potential presence of Tet enzymes in heterochromatin to catalyze 5hmC production in *Dnmt3a*-KO HSPCs (Fig. 4d–f). Similar features emerged in WT-old HSPCs, where deregulation of DNA methylation and increased 5hmC deposition at heterochromatin were noted (Figs. 3d,e and 4a–c).

To further investigate whether DNA methylation deregulation due to Dnmt disruption is associated with subnuclear relocalization of H3K9me3-marked genomic regions, we performed IF staining of H3K9me3 in HSPCs obtained from MxCre and MxCre-*Dnmt3a*f/f mice[37] treated with pIpC (Fig. 4g). In addition, we treated WT-young HSPCs ex vivo for 10 days with a selective Dnmt1 inhibitor (Dnmt1i), GSK-3484862[38,39], mimicking Dnmt1 downregulation during HSPC aging (Extended Data Fig. 5h). We observed strong nucleoplasmic staining of H3K9me3 in both *Dnmt3a*-KO HSPCs and WT-young HSPCs treated with Dnmt1i (Fig. 4g,h), whereas such changes were absent in age- and gender-matched control groups (Fig. 4g,h). Functionally, Dnmt1i-treated WT-young HSPCs displayed reduction in colony formation (Fig. 4i). Meanwhile, we observed prominent upregulation of age-related genes, such as *Ccl5*, *Cxcl10*, *Irf7*, *Oas3* and *Isg15* involved in immunoinflammatory response (Fig. 2i,k), in the Dnmt1i-treated group but not the control group (Fig. 4j). Next, we performed ChIP-seq analysis of H3K9me3 in control and *Dnmt3a*-KO HSPCs (Extended Data Fig. 5i). We identified 1,894 differentially enriched regions between control (MxCre) and *Dnmt3a*KO HSPCs, representing only 0.9% (n = 204,045) of total analyzed regions (Extended Data Fig. 5j,k). Among these regions, 568 exhibited de novo changes in H3K9me3 enrichment (312 appeared and 256 disappeared), indicating a rather minor impact of Dnmt3a deletion on H3K9me3 genomic distribution. In summary, results from both genetic and pharmacological manipulations, along with unbiased integrative epigenomic analysis, suggest that H3K9me3-marked heterochromatin

is more prone to DNA methylation deregulation than euchromatin. DNA methylation deregulation in heterochromatin may enhance Tet2-mediated 5hmC deposition, potentially contributing to the spatial relocalization of H3K9me3-marked genomic regions in aged HSPCs (Fig. 4d), ultimately leading to their functional decline.

Tet2 regulates heterochromatin relocalization in aged HSPCs

Based on the above findings, it appears that the subnuclear distribution of H3K9me3-positive regions occurs in HSPCs with deregulated DNA methylation, including global DNA methylation loss and increased DNA methylation variation in heterochromatins as seen in two cases, aged HSPCs and HSPCs with Dnmt loss-of-function. In contrast, such spatial changes were not observed in aged *Tet2*KO HSPCs. These findings prompted us to posit that Tet2 might play a crucial role in regulating the subnuclear distribution of H3K9me3-positive regions in cells with compromised DNA (de)methylation homeostasis. To test this hypothesis, we treated *Tet2*KO-young HSPCs with DMSO or Dnmt1i[38] under in vitro culture condition for 10 days and then performed IF staining of H3K9me3. Similar to the results obtained in aged *Tet2*KO HSPCs, H3K9me3-positive regions remained at the nuclear periphery in *Tet2*KO-young HSPCs treated with DMSO or Dnmt1i (Fig. 4h), with the CFU count numbers remaining unaltered regardless of Dnmt1 inhibition (Fig. 4i). Unlike WT HSPCs, Dnmt1i treatment seemed to exert rather minor effects on the expression of selected age-related genes in *Tet2*KO HSPCs (Fig. 4j). These data converge to support a potential direct involvement of Tet2 in regulating the subnuclear localization of H3K9me3-positive regions in stem cells with defective DNA methylation machinery, arising from either aging or DNMT loss-of-function, which could ultimately alter HSPC function (Extended Data Fig. 5l).

Increased expression of ERVs and ISGs in aged HSPCs

Given that heterochromatin often marks repetitive elements, we examined the transcription of repetitive elements in HSPCs using both bulk RNA-seq and scRNA-seq datasets. Indeed, we observed notable transcriptional alterations in different types of repetitive elements (REs) in both WT and *Tet2*KO groups during HSPCs aging (Fig. 5a,b and Extended Data Fig. 6a–c). Compared to the *Tet2*KO group, more pronounced alterations in transcription of REs were observed in WT HSPCs during aging (Fig. 5a–c). Among all the REs, the transcription of ERVs was prominently upregulated during aging (Fig. 5a). We further confirmed this independently by measuring selected ERV expression using real-time qPCR (Fig. 5d).

Next, we performed Micro-C experiments[40] to further explore whether spatial relocalization of H3K9me3-positive regions could contribute to ERV upregulation. We first calculated the A/B compartment score across the whole genome as described[41]. Among all the age-related compartment alterations found in WT and *Tet2*KO HSPCs, we observed that the majority of alterations (88.3% and 74.6% in WT and *Tet2*KO, respectively) were located at B compartment as previously reported[41] (Fig. 5e). Furthermore, we detected more B compartment changes in WT HSPCs (n = 2,735) compared with those in *Tet2*KO HSPCs (n = 1,883) during aging (Fig. 5e). Among these regions, we only detected 581 overlapping genomic regions between the two groups, suggesting distinct compartment changes in WT and *Tet2*KO HSPCs during aging (Extended Data Fig. 6d). We further evaluated 5hmC

level and the transcriptional activities of repetitive elements within these H3K9me3-enriched regions. Consistent with 5hmC analysis results within heterochromatin, we observed an increased 5hmC at regions that experienced compartment shifts during aging (Extended Data Fig. 6e). In parallel, we observed marked upregulation of ERVs in WT-old HSPCs compared to the WT-young group within these regions (Fig. 5f). However, the expression of ERVs within the same analyzed regions remained largely unaltered in the *Tet2*KO groups (Fig. 5f). A similar analysis was applied to measure the expression levels of other repetitive elements, including LINE and SINE, at H3K9me3-marked regions with compartment shifts, but no significant differences were observed among all groups (Extended Data Fig. 6f). These data strongly suggest that age-related spatial relocalization of H3K9me3-positive regions correlates with ERV upregulation.

To further probe whether ERV upregulation directly contributes to HSPCs aging, we treated HSPCs with a reverse transcriptase inhibitor (RTi)[42] to suppress cytosolic DNA derived from ERV, which could trigger downstream inflammatory response. We confirmed a significant reduction of cytosolic DNA from selected ERVs in all groups upon RTi treatment, with a particularly pronounced effect observed in the WT-old group (Fig. 5d). Real-time qPCR analysis further confirmed significant downregulation of age-related ISGs identified from our RNA-seq analysis (Fig. 2k) in WT-old HSPCs (Fig. 5g). In comparison, the expression of ISGs remained mostly unaffected in other groups (WT-young, *Tet2*KO-young and *Tet2*KO-old) following RTi treatment (Fig. 5g). In addition, RTi treatment enhanced the colony-forming capability of WT-old HSPCs but seemed to only have minor or no effects on other groups (Fig. 5h). Collectively, these findings suggest that altered spatial redistribution of H3K9me3-marked heterochromatin is associated with augmented transcription of ERVs during HSPCs aging, which could subsequently activate intracellular innate immune response to upregulate ISGs, ultimately contributing to functional decline of aged HSPCs.

Discussion

In this study, we observed distinct effects of aging on both WT and Tet2-deficient HSPCs. Although young *Tet2*KO HSPCs exhibited a growth advantage over WT, the clonal expansion advantage became more pronounced in *Tet2*KO HSPCs under aging conditions. Our findings indicate that TET2 is predominantly found at H3K9me3-marked heterochromatin. It mediates spatial redistribution of H3K9me3-positive regions only when cells experiencing DNA methylation disruptions, such as aging-related DNA methylation loss or DNMT(s) deficiency. In young healthy cells, a fully functional DNA methylation machinery seems to protect H3K9me3-marked heterochromatin from being accessed by TET. These findings align with and supplement recent observation regarding the relocalization of DNMTs from heterochromatin to euchromatin in TET-deficient cells[20]. Our data underscore the coordinated actions between DNMTs and TETs in maintaining proper DNA methylation levels across different genome compartments, that is, heterochromatin and euchromatin, in mammalian cells. The loss of either DNMTs or TETs disrupts DNA methylation homeostasis in both heterochromatin and euchromatin. This imbalance can lead to aberrant transcription in coding regions and exacerbating genome instability in heterochromatin (for example, ERVs upregulation), culminating in the functional decline

of aged HSPCs. Our findings shed light on how two epigenetic enzymes, which control DNA methylation in the opposite directions and are often mutated in patients with CH and hematological neoplasms[15–17], can produce similar clonal expansion phenotypes in HSPCs.

We observed spatial redistribution of H3K9me3-positive regions in HSPCs when their DNA methylation machinery is impaired, evident in aged HSPCs, those depleted of *Dnmt3a* or when treated with a Dnmt1 inhibitor. Our data also support the role of Tet proteins, particularly Tet2, in mediating the subnuclear localization of H3K9me3-positive regions. However, the molecular mechanism by which TET facilitates the redistribution of H3K9me3-positive regions in *DNMT*-defective cells remains to be elucidated. TET proteins may physically engage certain heterochromatin binding proteins in the absence of DNMTs. Alternatively, DNMTs or 5mC binding proteins (such as MeCP2 or MBD1)[19] might restrict H3K9me3-marked genomic regions and their binding proteins, such as HP1 family members, within the heterochromatin compartment. Functionally, we noted that the subnuclear redistribution of H3K9me3-positive regions in aged HSPCs could enhance the transcriptional activities of repetitive elements, especially ERVs, thereby triggering innate immune responses. This response is marked by the upregulation of ISGs, leading to functional decline of aged HSPCs. The similar observation of resurrection of ERVs has been reported using an in vitro culture system in human stem cells derived from premature aging models[43]. Furthermore, we have demonstrated that suppressing cytosolic DNA derived from ERVs with an RTi can effectively dampen the innate immune response and restore the colony-forming ability of aged HSPCs. Although the current study focuses on dissecting how spatial relocalization of H3K9me3-positive regions leads to ERVs upregulation in aged HSPCs, such spatial relocalization might also contribute to other aging-related defects. For instance, this redistribution might increase mutational rates within heterochromatins in aged or malignant cells, as previously reported[8]. Additionally, the relocalization of genomic regions marked by H3K9 methylation modifications from perinuclear regions toward the nucleoplasm could disrupt the proper 3D genome structure, resulting in functional decline in aged HSPCs. Further studies are warranted to explore these possibilities.

Our findings suggest that Tet proteins are required to mediate the spatial positioning of H3K9me3-positive regions within the nuclei, which seems to be essential for maintaining the self-renewal potential of aged HSPCs. Nevertheless, Tet2 depletion in cells experiencing DNA methylation anomalies, such as aged HSPCs, does not equate to a complete restoration of proper cellular function. Since DNA methylation is instrumental in the regulation of transcriptional activity and genome stability, cells without the proper DNA methylation machinery, such as *Dnmt*-TKO mESCs, are unable to differentiate in vitro[44]. Furthermore, Dnmt3a and Tet2 double-deficient HSPCs develop hematological malignancies[45]. Therefore, maintaining an intact epigenetic regulatory framework is paramount for preserving healthy cellular status.

In summary, using HSPCs as a model cellular system, we have illuminated key relationships between DNA (de)methylation dynamics and heterochromatin regulation during the aging process. These insights may extend to other conditions associated with DNA methylation imbalance, such as cancer and developmental defects.

Methods

Animal models

Animal studies were approved by the Institutional Animal Care Use Committee of the Institute of Biosciences and Technology, Texas A&M University (AUP 2020–0195). Most mouse strains bear a C57BL/6 genetic background unless otherwise noted. All the animals were housed in a certified animal facility with a standard dark/light cycle and a temperature- and humidity-controlled environment. *Tet2*$^{-/-}$[29], Mx1-Cre, Mx1-Cre *Dnmt3a*$^{f/f}$[37] mouse strains were reported previously. For genotyping, mouse tails were cut and boiled in 50 mM NaOH for 1 h and then neutralized in 10 mM Tris-HCl at pH 7.4. PCR was carried out using EmeraldAmp GT PCR Master Mix (TaKaRa). For acute *Dnmt3a* deletion, Mx1-Cre and Mx1-Cre *Dnmt3a*$^{f/f}$ mice were treated with 200 μg pIpC every other day via intraperitoneal (i.p.) injection for 10 days. Four weeks after injection, the deletion efficiency was measured by genotyping of targeted loci using the peripheral blood samples. Both male and female mice were used in this study.

Bone marrow cell isolation and LSK (Lin$^-$cKit$^+$Sca1$^+$) cell purification

Femurs and tibias were freshly isolated from mice and triturated using Hanks' Balanced salt solution without Ca^{2+} and Mg^{2+}. The cell suspension was further filtered with 40-μm cell strainers (Falcon) and treated with ACK (ammonium–chloride–potassium) lysis buffer to deplete red blood cells. Cells were stained with biotin conjugated lineage-specific antibodies (B220, Ter119, CD11b, Gr-1 and CD3e; 1:10 dilution). Lin$^-$ cells were isolated using anti-biotin microbeads (Miltenyi Biotec) through negative selection by following the manufacturer's instructions. For LSK cells purification, Lin$^-$ cells were further labeled with an APC conjugated cKit antibody (1:100) and a PE-CY7 conjugated Sca1 (1:100) antibody, followed by cell sorting using a BD Biosciences FACSFusion Cell sorter.

Flow cytometry analysis

Bone marrow cells were freshly isolated from femurs. Erythroid lineages were analyzed before depletion of red blood cells using PE-Ter119 and FITC-CD71 antibodies. For other lineage analysis, cells were removed with red blood cells and stained with PacBlue-CD4, PacBlue-CD8a, PacBlue-B220, PE-B220, PE-Gr-1 and PE-CD11b antibodies (BioLegend). For hematopoietic stem cells analysis, cells were labeled with a biotin conjugated anti-mouse lineage cocktail (CD19, B220, Ter119, CD11b, Gr-1 and CD3e; BioLegend), followed by staining with antibodies against PacBlue-streptavidin, APC-cKit, PE-Cy7-Sca1, PE-CD150 and FITC-CD48. For hematopoietic progenitor cells, PE-CD16/32 and FITC-CD34 antibodies were used instead of PE-CD150 and FITC-CD48. For reconstitution efficiency analysis, cells were stained with APC-CD45.2, FITC-CD45.1, PE-CD11b, PE-Gr-1, PacBlue-CD4 and PacBlue-CD8a using FACS buffer. All flow cytometry analyses were performed using an LSRII flow cytometer (BD Biosciences), and the data were analyzed using FlowJo v.10 (TreeStar). All antibodies used for flow cytometry were diluted with a 1:100 ratio.

EdU labeling

Mice were weighted and injected with EdU (40 ng g^{-1}) for 24 h. After depletion of red blood cells, bone marrow cells were stained with antibodies against surface markers, including APC-cKit, PE-Cy7-Sca1, PE-CD150 and FITC-CD48 (1:100 dilution). EdU was labeled using a Click-iT Plus EdU Alexa Fluor 350 Flow Cytometry Assay Kit (Thermo Fisher, #C10645) after fixation, permeabilization and blocking.

BMT

For repopulation assays, 0.1 million $CD45.2^+$ Lin^- or 250 LSK ($Lin^-cKit^+Sca1^+$) bone marrow cells from age- and gender-matched WT-young (4–8 weeks), *Tet2*KO-young (4–8 weeks), WT-old (18–24 months) or *Tet2*KO-old (18–24 months) mice were co-transplanted with bone marrow cells purified from gender-matched B6.SJL-PtprcaPepcb/BoyJ ($CD45.1^+$) mice (4–8 weeks) with a 1:10 ratio (with red cell depleted). Cell mixtures were injected into lethally irradiated C57BL/6 mice. For competitive assays, WT LSK cells ($n = 900$) from age-matched (young or old) mice were mixed with *Tet2*KO LSK cells ($n = 100$) in a ratio of 9:1 and injected into lethally irradiated C57BL/6 mice. Peripheral blood was analyzed 4–6 weeks after transplantation biweekly to monitor engraftment efficiency and lineage commitment.

For the secondary BMT experiment, 1 million total bone marrow cells isolated from the mice transplanted with *Tet2*KO LSKs (young or old) were used as donor cells and injected into lethally irradiated CD45.1 recipient mice.

In vitro CFU assay

LSK cells ($n = 250$ cells) were isolated from the indicated groups. Cells were plated in triplicate in cytokine-supplemented methylcellulose medium supplemented with mSCF, mIL3, hIL6 and hEPO (MethoCult GF M3434; StemCell Technologies). The number of total cells and colonies was counted 10 days after culture, and the same number of cells were replated in MethoCult M3434 media for up to four rounds.

Ex vivo HSC culture and inhibitor treatment

HSCs were cultured in a medium composed of F12 medium, 10 mM HEPES, 1% ITSX, 1% P/S, 1% glutamine, 100 ng ml^{-1} mouse TPO, 10 ng ml^{-1} mouse SCF and 0.1% PVA based on a previous publication[46]. For the inhibitor treatments, HSCs were cultured with 50 nM Dnmt1 inhibitor[38] (GSK-3685032, MedChemExpress, HY-139664) or 400 μM reverse transcriptase inhibitor[42] for 10 or 5 days, respectively. Media and inhibitors were changed every 2 days.

Histological analysis

Spleen, liver and lung tissues were collected from the recipient mice and fixed with 4% paraformaldehyde. Cardiac tissues were fixed with 10% FA for 24 h. Fixed tissues were dehydrated using gradient alcohol and xylene. Tissue blocks were embedded in paraffin and cut into 5 μm sections for hematoxylin and eosin staining. Images were taken using a Nikon Eclipse Ci microscopy.

Dot-blot analysis

DNA was purified using a QIAamp DNA Micro Kit (Qiagen). Two-fold serial diluted DNA samples were denatured in 0.4 M NaOH, 10 mM EDTA at 95 °C for 10 min, followed by neutralization with ice-cold 2 M ammonium acetate (pH 7.0). After incubating on ice for 10 min, denatured DNA samples were spotted onto a 0.22-μm nitrocellulose membrane by using an assembled Bio-Dot apparatus (Bio-Rad). The membrane was washed with 2xSSC buffer, air-dried and crosslinked through vacuum-baking at 80 °C for 2 h. After hybridization, the membrane was blocked with 5% BSA at room temperature for 1 h and incubated with a primary anti-5hmC antibody (1:3000, Active Motif #39769) overnight at 4 °C. The next day, the membrane was incubated with an anti-rabbit HRP-conjugated secondary antibody (1:3,000, Cell Signaling, #7074 S) at room temperature for 1 h. After visualization using West-Q Pico Dura ECL Solution (GenDepot), the membrane was stained with 0.02% methylene blue in 0.3 M sodium acetate (pH 5.2) to ensure equal loading of DNA samples. Images were visualized through the ChemiDoc Imaging System (Bio-Rad) and data were processed by Image Lab software.

Western blot analysis

Histones were extracted from nuclei according to the standard acid-extraction protocol. For others immunoblotting, RIPA buffer (150 mM NaCl, 1% TritonX-100, 0.1% SDS, 0.5% sodium deoxycholate and 50 mM Tris-HCl, pH 8.0) was used to lyse cell pellets. The lysates were loaded to SDS-PAGE (4% to 12% gradient; GenScript) gels by mixing with 1xSDS loading buffer (100 mM Tris-Cl, 4% SDS, 0.2% bromophenol blue, 20% glycerol and 200 mM DTT, pH 6.8) after denaturation at 95 °C for 10 min. Proteins were transferred using nitrocellulose membranes (Millipore) and blocked in 5% BSA for 1 h at room temperature. Membranes were then incubated with the corresponding primary antibodies at 4 °C overnight, followed by incubation with a secondary antibody at room temperature for 1 h. The antigen-antibody complexes were visualized through the ChemiDoc Imaging System (Bio-Rad) by using West-Q Pico Dura ECL Solution (GenDepot). The data were processed by Image Lab software.

IF staining

LSK cells were purified by cell sorting as described above and concentrated onto poly-D-lysine-precoated microscope slides through Cyto-spin. The cells were fixed with freshly prepared 4% paraformaldehyde solution for 15 min at room temperature. After washing three times with PBS, cells were permeabilized with 0.2% Triton X-100 in PBS, followed by blocking with 1% BSA/0.05% Tween-20/ PBS at room temperature for 1 hr. Then cells were incubated with primary antibodies in a blocking buffer overnight at 4 °C. Cells were then washed three times with PBS and incubated with secondary antibodies in the blocking buffer at room temperature for 1 h. Cells were then covered with antifade mountant (with DAPI) for further imaging. Antibody information: anti-H3K9me3 (1:500, Abcam #ab8898), anti-H3K9me2 (1:500, Active Motif #39239), anti-H3K4me3 (1:500, Abcam #ab8580), anti-Lamin B1(1:500, Abcam #ab16048), anti-H3K27Ac (1:500, Abcam #H3K27Ac), anti-rabbit Alexa Fluor 568 (1:1,000, Invitrogen #A-11011), anti-mouse Alexa Fluor 647 (1:1,000,

Invitrogen #A-21235). A W1 Yokogawa Ti2 Nikon spinning disk confocal microscope and Nikon NIS-Elements AR software were used for image acquisition and analysis.

Human CD34$^+$ bone marrow cells isolation and IF staining

Human CD34$^+$ cells were purified from human bone marrow aspirates using human CD34 microbeads (Miltenyi Biotec, #130–046-702). CD34$^+$ cells were concentrated onto poly-D-lysine precoated microscope slides. Cells were fixed with 100% methanol for 30 min at 4 °C and then permeabilized with TBST at room temperature for 25 min. Antibody incubation and image analysis were performed as described above in the IF staining section.

Nuclear/cytoplasmic DNA purification

Nuclear/cytoplasmic fractions were obtained using a nuclear/cytosol fractionation kit (Abcam, #ab289882). DNA was purified from extracts through ethanol precipitation after treatment with 20 mg ml^{-1} RNase A (30 min at 37 °C), 20 mg ml^{-1} proteinase K (1 h at 55 °C), and phenol/chloroform extraction. Purified DNAs were dissolved in water and used for the downstream qPCR analysis. To calculate the relative expression, the cytoplasmic DNA was normalized to nuclear DNA using primers specific to nuclear *Tert*.

RNA isolation and RT-qPCR

Total RNA was obtained using an AllPrep DNA/RNA Micro Kit (Qiagen) by following the manufacturer's instructions. DNA was removed through DNase I digestion. cDNA synthesis was achieved using a PrimeScript first-strand cDNA Synthesis Kit (Takara). Gene expression was quantified on ViiA 7 Real-Time PCR System (Applied Biosystems) using 2× Universal SYBR Green Fast qPCR Mix (ABclonal). Primers used for RT-qPCR were listed in Supplementary Table 6.

RNA-seq library preparation and data analysis scRNA-seq.

Lin$^-$ cells were isolated with libraries subsequently generated by using the Chromium Single-Cell 3′ Reagent V2 Kit (10x Genomics) following the manufacturer's instructions. Briefly, GEMs containing a single cell were generated, followed by the production of barcoded, full-length cDNA from poly-adenylated mRNA. Then the cDNA was amplified and enzymatically fragmented. Final libraries were constructed through end repair, A-tailing, adaptor ligation and amplification with index primers. Multiplexing indexed libraries were pooled and sequenced on a Hiseq 3000 Platform (Illumina) with a paired-end, double indexing format and 150/8/8/150-bp read length.

Cellranger (v6.0.0) was used to demultiplex the raw sequencing data, generate fastq files and align the fastq files to mm10 genome. The unique molecular identifier (UMI) counting and barcode decoding for each cell were achieved by using Cellranger. The raw reads count matrix with row as genes and column as cells were input to SCANPY pipeline[47] to perform quality control and the downstream analysis. For coding gene analysis, cells with more than 10% mitochondrion reads and less than 100 genes were discarded. Genes detected in less than 50 cells were also removed. For pseudotime analysis, we used scVelo[32] with default settings to infer the future gene expression dynamics in each cell. For scTE analysis, we filtered out cells detected with less than 300 genes and less than 30,000 UMIs. Genes

expressed in less than 100 cells were discarded. SCANPY was used to normalize the count matrix (normalize_total function) and the top 4,000 most highly variable genes were used for principal-component analysis (PCA), and the first 30 principal components were used for UMAP analysis.

Bulk RNA-seq with ultra-low input of RNA.

Total RNA was extracted from mouse LSK bone marrow cells using an AllPrep DNA/RNA Micro Kit (Qiagen), with the concentration determined by a Qubit 4 fluorometer using a Qubit RNA High Sensitivity Assay Kit. The same amount of total RNA was proceeded for the first-strand cDNA synthesis and cDNA amplification following the manufacturer's protocol provided by the SMART-Seq v4 Ultra Low Input RNA Kit (Takara). Amplified cDNA qualities were determined by using the Agilent 2100 Bioanalyzer and Agilent's High Sensitivity DNA Kit. Library preparation was achieved by using the SMART-Seq Library Prep Kit (Takara). For bulk RNA-seq analysis, STAR (2.7.0a) was used to align raw reads on mm10 genome (UCSC). Uniquely mapped reads were kept for calculation of gene counts using htseq-count from HTSeq package. Normalization of gene counts and identification of DEGs were performed by using DESeq2. TEtranscripts (26206304) was used for the quantification of TE's expression from bulk RNA-seq data.

CMS-IP-seq library preparation and data analysis

CMS-IP-seq was used for genome-wide 5hmC analysis as previously described[21,22]. 100–1,000 ng genomic DNA was spiked in with 0.5% unmethylated lambda DNA and 5% H9 human genomic DNA and sheared into 200–400 bp DNA fragments using a Covaris M220 Focused-ultrasonicator. Sonicated DNA were incubated with CMS-specific antiserum pre-conjugated protein A/G dynabeads after bisulfite treatment. CMS-containing DNA fragments were further denatured with NaOH/EDTA and immunoprecipitated, followed by library generation using Pico Methyl-Seq Library Prep Kit (Zymo Research) according to the manufacturer's instructions. Multiplexing indexed libraries were pooled and quantified by Kapa library quantification kit and sequenced on the Illumina NextSeq 500 platform with single-end, 80/6/0/0 mode, aiming to get 30 million reads per library.

For CMS-IP-seq analysis, we first aligned raw reads to mm10 using BSMAP[48]. Only uniquely mapped reads were retained for the downstream analysis. A CMS count table was tabulated for the 5hmC-enriched regions detected by MACS2 (ref. 49). To facilitate the visualization of 5hmC signals, bigWig files for read coverage normalized by a factor of 10^9 were generated from the aligned BAM files and visualized in the UCSC genome browser. Diffbind[50] with edgeR as the selected method was applied to identify differentially enriched regions in CMSIP-seq analysis among the analyzed groups.

WGBS library preparation and data analysis

Genomic DNA (10–100 ng) that purified from mice LSK cells were spiked in with 0.5% lambda DNA and treated with bisulfite conversion by using an EZ DNA methylation-lightning kit (Zymo Research). The bisulfite treated DNA was further used for library preparation using Accel NGS Methyl Seq DNA Library Kit according to the manufactures'

instructions. Pooled DNA libraries were sequenced on Illumina Nova-seq platform with paired end, 150/8/8/150 mode.

Raw fastq files were mapped to the mm10 genome assembly using bsmap-2.89 software with '-v 6 -n 1 -q 3 -r 1' parameters. The bisulfite conversion ratios were estimated using unmethylated lambda DNA. Mcall modual in model based analysis of bisulfite sequencing data (MOABS)[51] was used to call the mCG/CG ratios for each CpG site. The CpGs with coverage ≥5 was used for downstream analysis. Mcomp modual was used to call DMRs with parameter '–minNominalDif=0.2–minDmcsInDmr 3–maxDistConsDmcs 500'. For each 10-k bin with H3K9me3 enrichment signals, we first calculated the differential DNA methylation ratios for each CpG between two groups within it and then calculated the standard deviation of differential DNA methylation level of these CpGs within each 10-k bin. The *P* value for age-related DMR (Supplementary Table 5) was calculated by using hypergenometric test with two sides and was Bonferroni corrected.

H3K9me2/3 ChIP-seq library preparation and data analysis

LSK cells (0.1 million) from the corresponding experimental groups were mixed with 5% human HEK293T cells and subjected to crosslinking and sonication as previously described[52]. Subsequently, the cell lysates were incubated with H3K9me2 (Abcam, #ab1220) or H3K9me3 (Abcam, #ab8898) antibody-conjugated magnetic beads overnight at 4 °C. On the following day, the magnetic beads were washed five times with wash buffer (50 mM HEPES-KOH, 500 mM LiCl, 1 mM EDTA, 1% NP-40 and 0.7% Na-deoxycholate, pH 7.5) and then washed twice with 1X TE buffer before elution. After reverse crosslinking, the chromatins were eluted, and both input DNA and immunoprecipitated DNA underwent library preparation using the Takara ThruPLEX DNA-seq kit (R400674), following the manufacturers' instructions.

H3K9me2 and H3K9me3 ChIP-seq raw data were mapped to mm10 genome using bowtie2 and the uniquely mapped reads were used for downstream analyses. Enriched domain detector[53] was designed to detect wide genomic enriched domains, such as H3K9me2 and H3K9me3 ChIP-seq data. We used 10-k bin size to calculate the H3K9me2 and H3K9me3-enriched signal compared with input using enriched domain detector. The $\log_2$ ratio fold-change against input was used to generated bigwig files which can be visualized using the Integrative Genomics Viewer[54]. Diffbind[50] with edgeR as selected method to identify differentially enriched regions of H3K9me3 ChIP-seq analysis between different groups.

Micro-C sequencing

LSK cells (0.5 million) were harvested from WT-young, WT-old, T2KO-young and T2KO-old mice. The libraries were generated using a Dovetail Micro-C Kit according to the manufacturer's instructions. In brief, cells were crosslinked with FA in the presence of DSG, followed by in situ MNase nuclease digestion and cell lysis. Then, chromatins were captured by chromatin bind beads for future end polishing, bridge ligation, intra-aggregate ligation and reverse crosslinking. The purified DNA was processed with library generation. Micro-C pipeline (https://micro-c.readthedocs.io/en/latest/) was used to analyze the Micro-C data. Specifically, we used bwa (0.17.17) to align raw reads on mm10 genome, and the properly

mapped read pairs were retained for downstream analysis. For each sample, mapped.pairs file was used as input for juicer_tools_1.22.01 to generate contact maps (hic format file). hicPCA function from HiCExplorer (3.7.2) with H3K4me3 ChIP-seq tracks of HSCs from young (4-month-old) mice as correction for PCA values was applied to determine A/B compartment regions.

Statistics and reproducibility

The exact value of *n* biologically independent samples are included in figure legends. Data are presented as mean values ± s.d. Two-tailed Student's *t*-test was performed for comparisons between two groups. One-way or two-way ANOVA was used for the comparisons between multiple groups. All of them were performed using GraphPad Prism software (version 9). Two-sided Kolmogorov-Smirnov tests were performed for all the violin plots and boxplots. For all the boxplots, the bounds of the box span from the 25th to 75th percentile, and the center line within box represents median. Whiskers represent median ± 1.5 times interquartile range. Dots represent outliers. The upper most line/dots represent the maximum value, and the lowest line or dots represent the minima value. For animal experiments, no statistical methods were used to predetermine sample sizes, although sample sizes were consistent with those from previous studies[55]. No randomization method was used to allocate animals to experimental groups. Data distribution was assumed to be normal, but this was not formally tested. Data collection and analysis were not performed blind to the conditions of the experiments.

Reporting summary

Further information on research design is available in the Nature Portfolio Reporting Summary linked to this article.

Extended Data

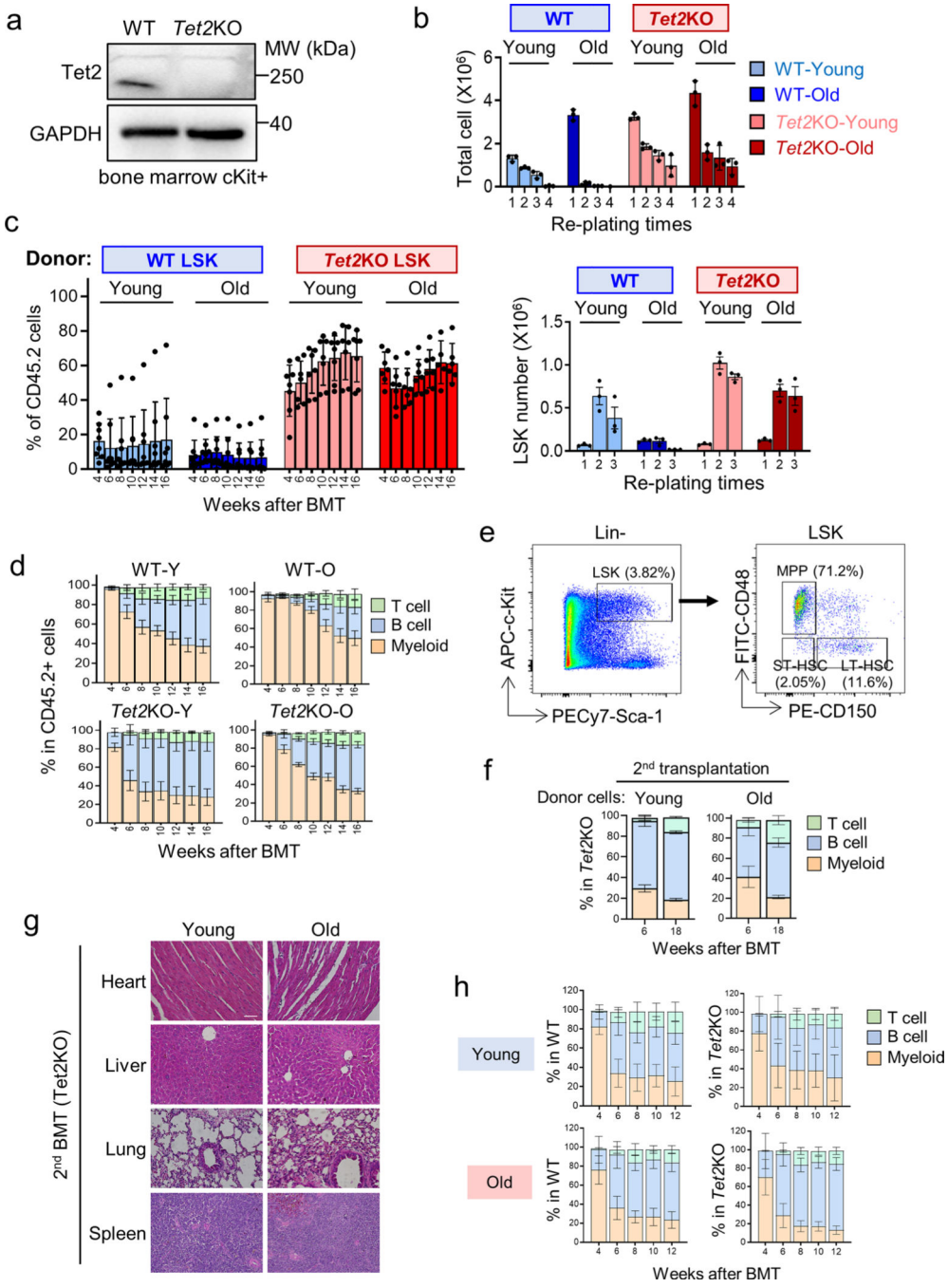

Extended Data Fig. 1 |. Tet2 depletion mitigates age-related decline in HSPC self-renewal and repopulation capability (Related to Fig. 1).

a, Immunoblot analysis of Tet2 expression in cKit+ cells from bone marrow of WT or *Tet2*KO mice (6 ~ 8-week-old, n = 3 male and 2 female mice). **b**, The total cell numbers (Top) and the fraction of LSK cells (Bottom) in the indicated replating times. CFU assay was used to assess HSPCs function. Data are shown as mean ± S.D; n = 3 biological replicates. (Two-way ANOVA test; Supplementary Table 1). **c**, The reconstitution efficiency

of lethally irradiated CD45.1 mice transferred with Lin$^-$cKit$^+$Sca1$^+$ (LSK) cells (n = 3 male and 2 female donor mice / group). The reconstitution efficiency was measured biweekly from the peripheral blood till 16 weeks post-BMT (n = 5–7 recipient mice with equal number of male and female mice / group, each dot represents an individual recipient mouse). (Two-way ANOVA test; Supplementary Table 1). **d**, Lineage analysis in the peripheral blood collected from lethally irradiated CD45.1 mice transferred with LSK cells (n = 5–7 recipient mice /group, each dot represents an individual recipient mouse). Data are shown as mean ± S.D. (Two-way ANOVA test; Supplementary Table 1). **e**, The gating strategies. Lin$^-$, lineage-negative; LSK, Lin$^-$cKit$^+$Sca1$^+$; LT-HSC, long-term HSC; MPP, multipotential progenitor; ST-HSC, short-term HSC. **f**, Lineage analysis in the peripheral blood collected from recipient mice undergoing a second bone marrow transplantation using donor cells from the recipient mice transferred with young and old *Tet2*KO HSPCs listed in Extended Data Fig. 1c, d. Data are shown as mean ± S.D. (n = 3 male donor mice and 3–5 male recipient mice / group). **g**, Representative Hematoxylin and Eosin (H&E) stained sections of heart, liver, lung, and spleen tissues collected from the CD45.1 recipient mice with secondary BMT (18 weeks post-BMT). Donor cells were total bone marrow cells isolated from mice transplanted *Tet2*KO LSKs (young or old) as shown in Extended Data Fig. 1c, d (n = 3 donor mice). Scale bar, 200 μm. **h**, Lineage analysis in the peripheral blood collected from the recipient mice transferred with mixed HSPCs as shown in Fig. 1e. Data are shown as mean ± S.D. (Two-way ANOVA test; Supplementary Table 1).

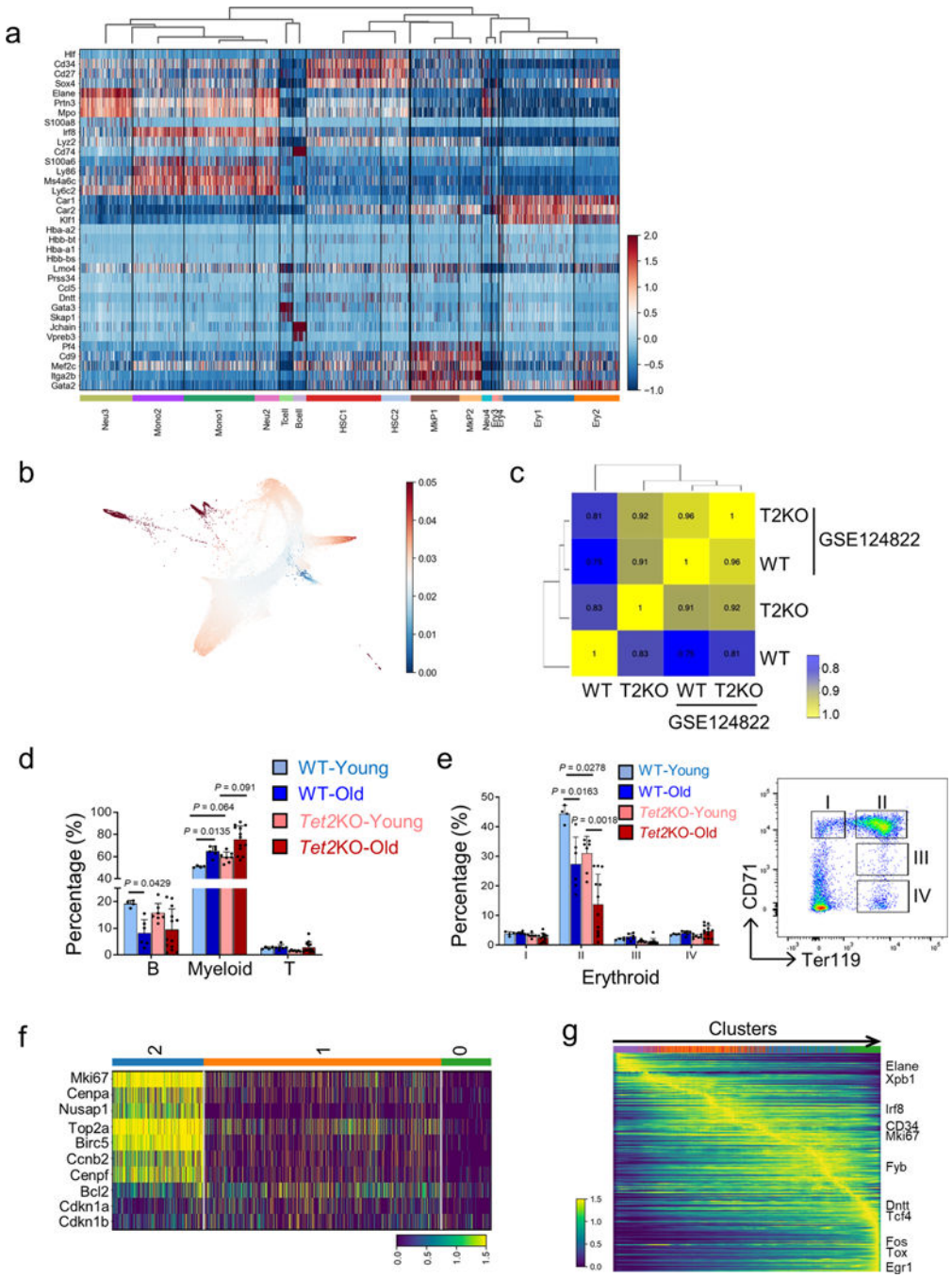

Extended Data Fig. 2 |. Distinct transcriptional changes during WT and *Tet2*KO HSPCs aging (Related to Fig. 2).

a, Heatmap showing the expression of the marker genes used to annotate cell populations. **b**, Pseudotime inference reveals the differentiation process projected in UMAP-based embedding (shown in Fig. 1a) in all the analyzed cells. Dark blue represents cells in earlier differentiation stages; while dark red represents cells in later differentiation stages. **c**, The cell type ratio correlation analysis of scRNA-seq data collected in this study (WT-Young and *Tet2*KO-young) with the previously published dataset (GSE124822). **d**, Lineage analysis

in the bone marrow collected from gender- and aged-matched congenic WT-young, WT-old, *Tet2*KO-young, and *Tet2*KO-old mice. Young, 6–8 weeks; Old, 18–24 months. Data are shown as mean ± S.D; n = 4–13 (equal number of male and female mice) / group, each dot represents an individual mouse. (Two-tailed Student's *t*-test). **e**, (Left) Erythroid lineage analysis on bone marrow cells collected from gender- and aged-matched congenic WT-young, WT-old, *Tet2*KO-young, and *Tet2*KO-old mice. Data are shown as mean ± S.D; n = 4–12 (equal number of male and female mice) / group, each dot represents an individual recipient mouse (Two-tailed Student's *t*-test). (Right) The gating strategies of erythroid progenitors. **f**, Heatmap showing the expression of marker genes used to annotate cell cycles. **g**, Heatmap representing genes associated with the pseudotime trajectory for HSC as shown in Fig. 2e.

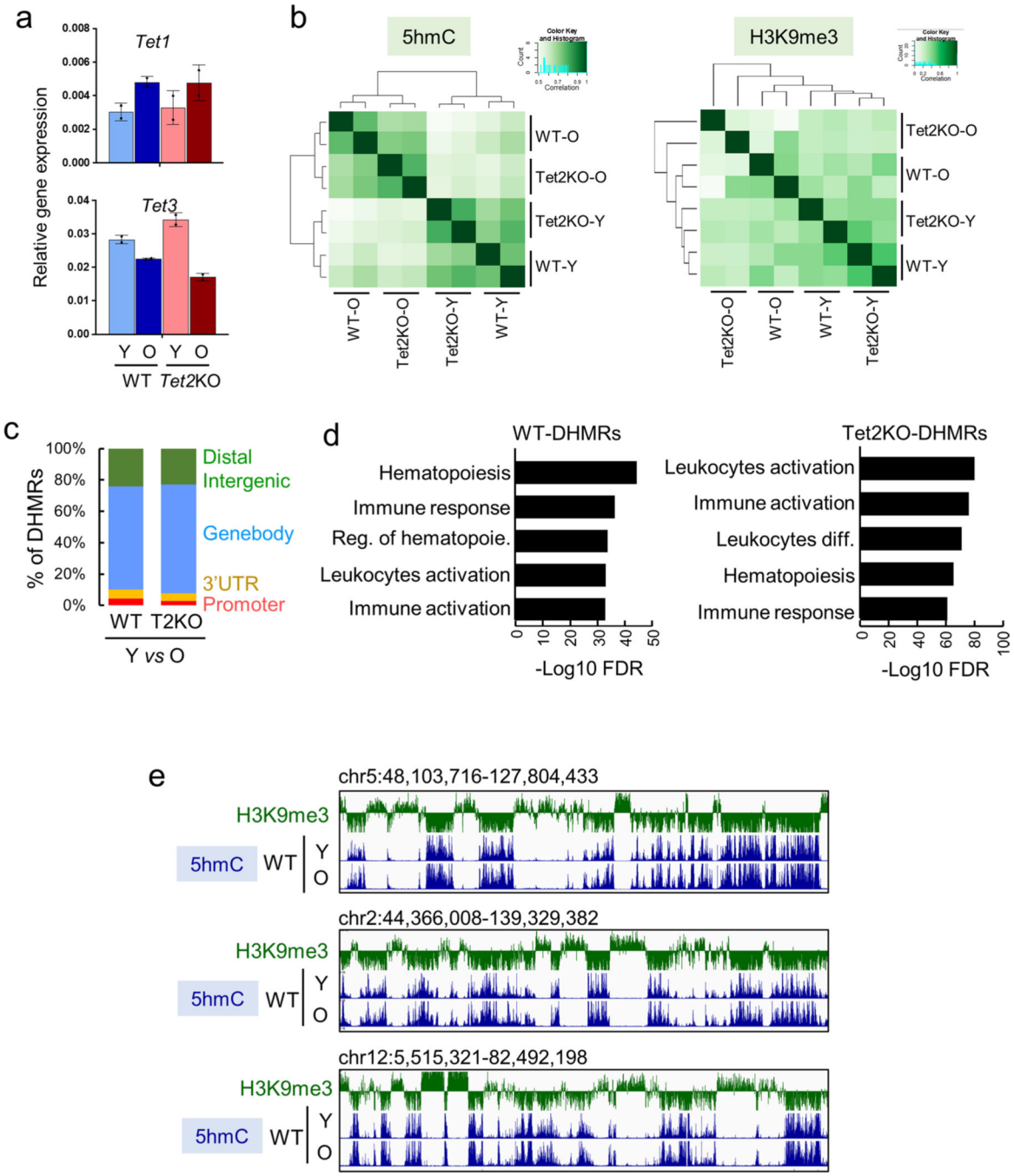

Extended Data Fig. 3 |. Measurements of Tet expression and 5hmC in young and aged HSPC (Related to Fig. 3).

a, RT-qPCR analysis of *Tet1* and *Tet3* expression in LSK cells from WT-young, WT-old, *Tet2*KO-young, and *Tet2*KO-old mice. Data are shown as mean ± S.D (n = 3 independent experiments). **b**, Summary of Pearson's correlation coefficients of 5hmC (left) and H3K9me3 (right) in the indicated groups. **c**, The percentage of age-related DHMRs in various genomic regions (distal, intergenic, genebody, 3'UTR, or promoter regions) for the indicated comparison groups (left, WT-Young vs WT-Old; right, *Tet2*KO-Young vs *Tet2*KO-

Old). **d**, The top 5 enriched biological functions of age-related DHMRs identified from WT or *Tet2*KO HSPCs (young vs old) using the GREAT analysis. **e**, The genome browser views of 5hmC (blue, CMSIP) (scale: 0 to 5) in LSK cells purified from WT-young and WT-old mice. H3K9me3 track (scale: −0.5 to 0.5) in LSK cells purified from the WT-young group is used as the reference to discriminate between heterochromatin and euchromatin.

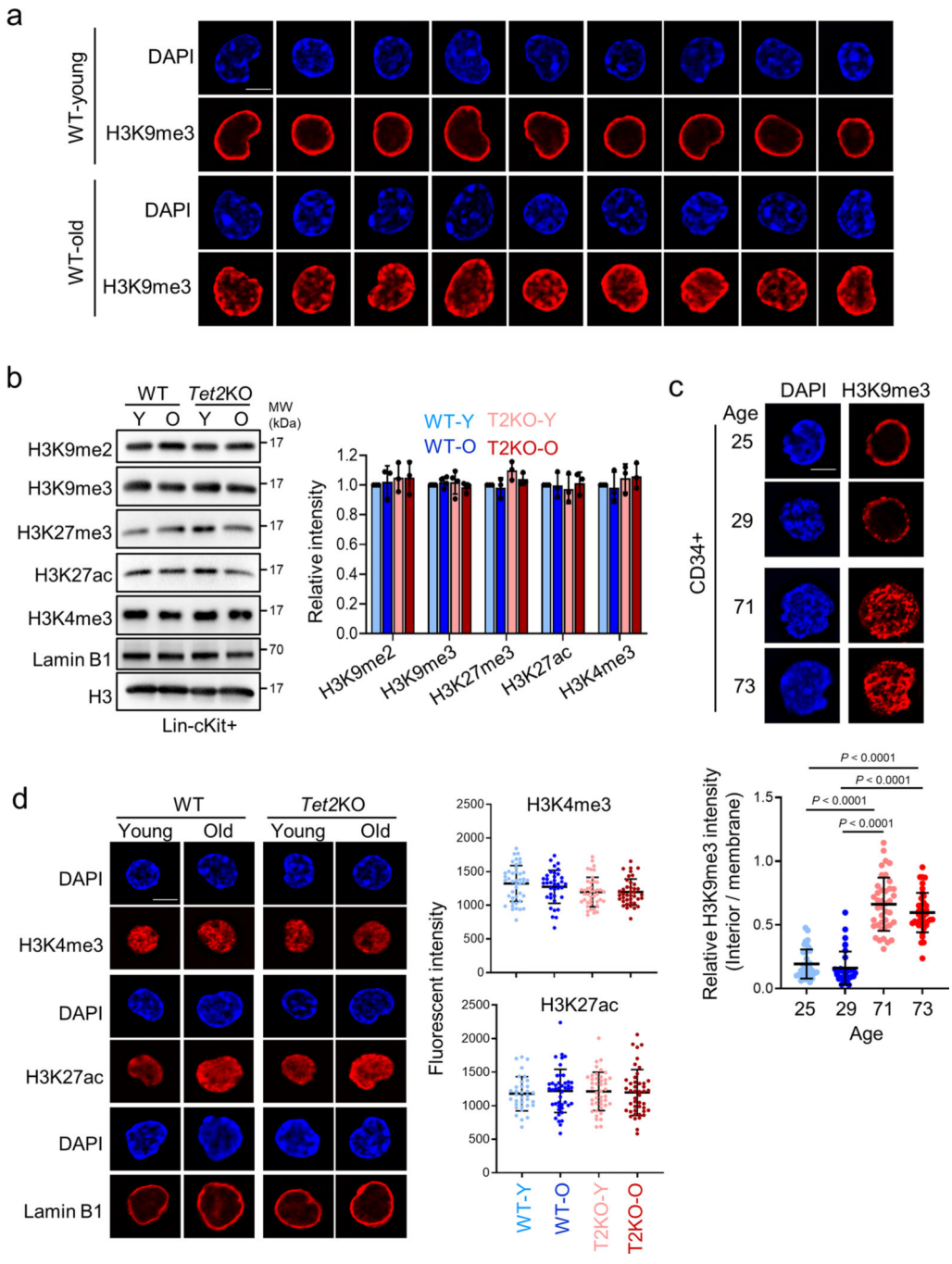

Extended Data Fig. 4 |. Tet2 loss prevents the spatial relocalization of H3K9me3-marked heterochromatin from the nuclear periphery to the nucleoplasm during HSPC aging (Related to Fig. 3).

a, Additional representative images of immunofluorescence (IF) staining of H3K9me3 in LSK cells purified from WT-young (6–8 weeks old) and WT-old (18 months old) mice. DAPI was used to stain the whole nuclei. Scale bar, 5 μm. **b**, Immunoblot analysis (left) and quantification (right) of the indicated histone marks in LK cells purified from WT-young, WT-old, *Tet2*KO-young, and *Tet2*KO-old mice. Data are shown as mean ± S.D; n = 3 independent biological replicates. **c**, Immunofluorescence analysis (top) and quantification (bottom) of H3K9me3 in CD34+ cells purified from human bone marrow at the indicated ages. Data are shown as mean ± S.D; n = 35–40 cells, Scale bar, 5 μm. **d**, (Left) Immunofluorescence staining of H3K4me3, H3K27ac, and lamin B1 in LSK cells. Scale bar, 5 μm. (Right) The quantification of fluorescence intensities of H3K4me3 and H3K27ac. Data are shown as mean ± S.D; n = 35–45 cells (n = 3–10 mice with equal number of male and female mice).

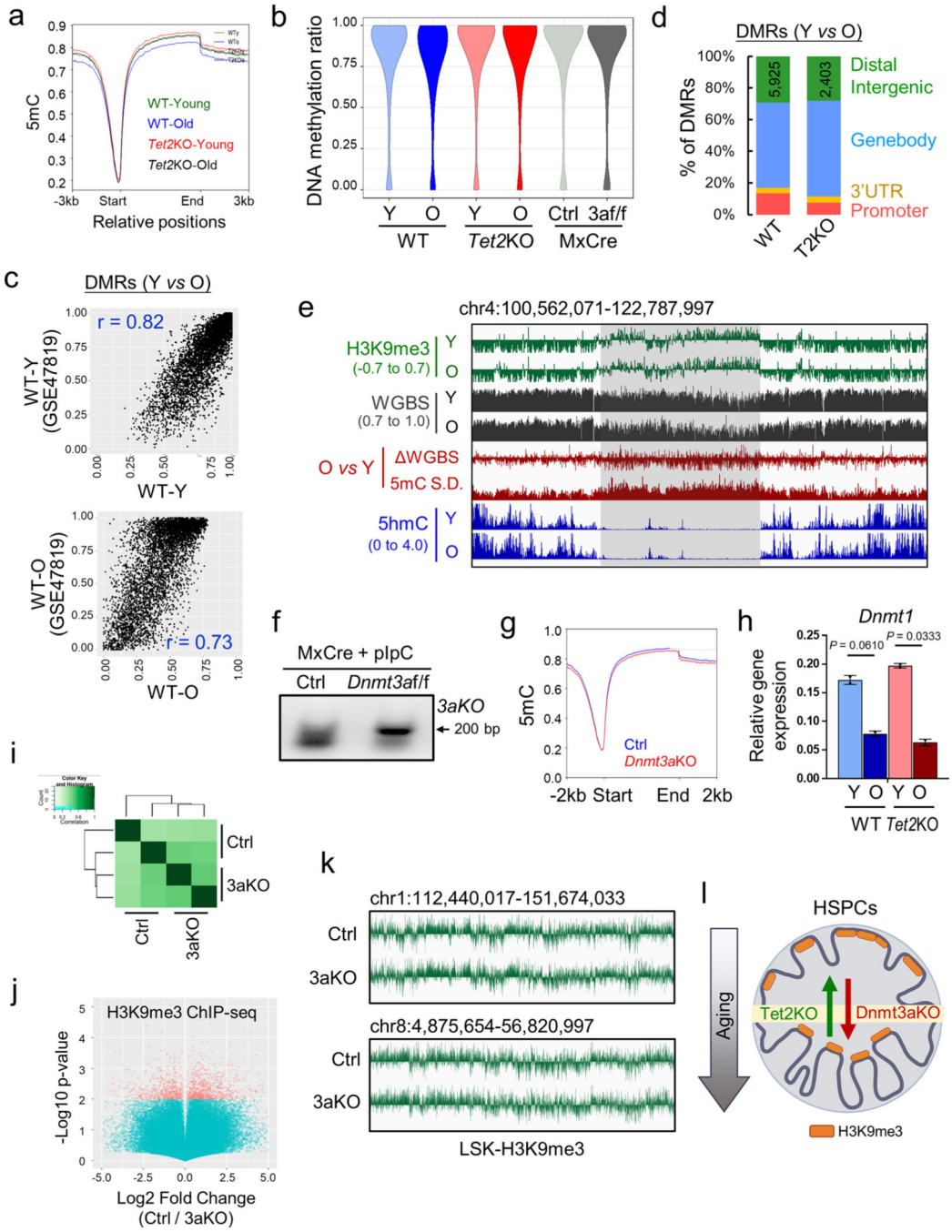

Extended Data Fig. 5 |. DNA methylation deregulation contributes to the spatial relocalization of H3K9me3 in HSPCs. (Related to Fig. 4).

a, Average DNA methylation levels within the coding regions in LSK cells purified WT-young (6–8 weeks), WT-old (18 months), *Tet2*KO-young (6–8 weeks), and *Tet2*KO-old (18 months) mice. **b**, Violin plot of DNA methylation levels in the indicated groups. **c**, Scatterplot of age-related DMRs (young *vs* old) identified from WGBS data in this study and the published WGBS data (GSE47819). The Pearson's correlation coefficients were listed to compare the DNA methylation levels within age-related DMRs for the

indicated groups. **d**, Genomic distribution of age-related DMRs (young *vs* old) identified from WT and Tet2KO groups. **e**, Genome browser views illustrating H3K9me3, WGBS, 5mC changes (Δ5mC), the standard deviation of 5mC changes (5mC S.D.), and 5hmC in WT-young and WT-old HSPCs. **f**, PCR-based genotyping results using genomic DNA isolated from the tails collected from MxCre and MxCre-Dnmt3a$^{f/f}$ mice treated with pIpC. Genotyping was performed 4 weeks after pIpC treatment. **g**, Average DNA methylation levels within the coding regions in LSK cells purified from MxCre (blue) and MxCre-Dnmt3af/f mice (red) treated with pIpC and analyzed 4 weeks after pIpC treatment. **h**, RT-qPCR analysis of *Dnmt1* expression in LSK cells purified from WT-young, WT-old, *Tet2*KO-young and *Tet2*KO-old mice. Data are shown as mean ± S.D (n = 3). (Two-tailed Student's *t*-test). **i**, Summary of the Pearson's correlation coefficients of H3K9me3 ChIP-seq data for LSK cells purified from MxCre (control) or MxCre-Dnmt3a$^{f/f}$ (*Dnmt3a*KO) mice treated with pIpC. **j**, The scatterplot analysis to identify genomic regions exhibiting significant differential H3K9me3 enrichment between MxCre (control) and MxCre-Dnmt3a$^{f/f}$ (*Dnmt3a*KO) HSPCs. **k**, Genome browser view of H3K9me3 in LSK cells purified from MxCre (control) and MxCre-*Dnmt3a*$^{f/f}$ mice treated with pIpC. **l**, Schematic illustrating the impact of aging, Tet2 and Dnmt3a in regulating the spatial localization of H3K9me3-marked heterochromatin.

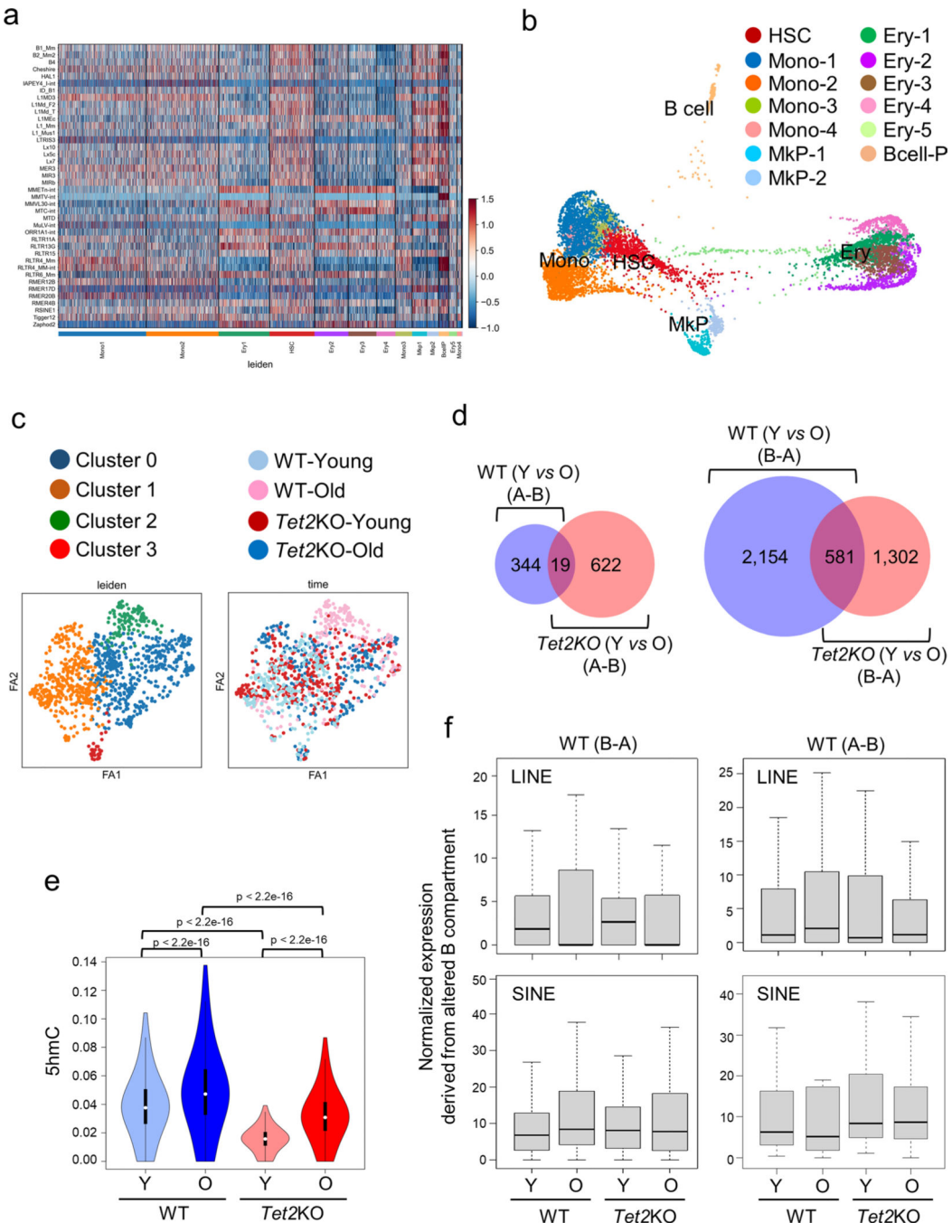

Extended Data Fig. 6 |. Upregulation of repetitive elements in aged HSPCs contributes to their functional decline (Related to Fig. 5).

a, Single-cell expression profiles of repetitive elements from each cell cluster in all the analyzed Lin¯ cells (n = 8,352). **b**, UMAP dimensionality reduction showing the cell distribution, taking into account the expression of repetitive elements as listed in Extended Data Fig. 6a, of all analyzed Lin¯ cells with high coverage (more than 300 genes and 30000 UMIs) (n = 8,352) purified from WT-young, WT-old, *Tet2*KO-young and *Tet2*KO-old mice. Young mice: 6–8 weeks old; Old mice: 18–24 months old. HSC, hematopoietic

stem cells; Mono, monocyte progenitor; Ery, erythroid progenitor; MkP, megakaryocyte progenitor; Bcell-P: B cell progenitors. **c**, (Left) UMAP dimensionality reduction (n = 929 cells) in HSCs identified from the analysis performed in panel A. Four distinct clusters were identified based on the gene expression signatures including repetitive elements listed in Extended Data Fig. 6b. (Right) UMAP plot showing the distribution of HSCs in the indicated groups. **d**, Venn diagram to illustrate the overlapping genomic regions with age-related compartment changes in WT and *Tet2*KO groups. **e**, Violin plot of 5hmC levels in H3K9me3-marked genomic regions with age-related compartment changes in the indicated groups. **f**, Normalized expression of SINE and LINE elements within H3K9me3-marked genomic regions with age-related compartment changes (B-to-A or A-to-B) in the indicated groups.

Supplementary Material

Refer to Web version on PubMed Central for supplementary material.

Acknowledgements

We are grateful for the Epigenetic core at the Institute of Biosciences and Technology at the Texas A&M University. This work was supported by grants from Cancer Prevention and Research Institute of Texas (RP210070 to Y.Z.), National Institute of Health grants (R35HL166557, R01DK132286 and R01CA240258 to Y.H.; R01CA232017 and R21CA277257 to Y.Z.; P01AG036695, DK092883, CA183252, P30CA125123 and P01CA265748 to M.A.G.), Leukemia & Lymphoma Society (LLS-TRP 6680-24 to Y.Z.) and the Welch Foundation (BE-1913-20220331 to Y.Z.).

Data availability

The sequencing datasets were deposited into the NCBI BioProject under the accession number GSE183675. The majority of data are available in the source data file. All other data supporting the findings of this study are available from the corresponding authors upon reasonable request.

References

1. Kramer A. & Challen GA The epigenetic basis of hematopoietic stem cell aging. Semin. Hematol 54, 19–24 (2017). [PubMed: 28088983]
2. Sun D. et al. Epigenomic profiling of young and aged HSCs reveals concerted changes during aging that reinforce self-renewal. Cell Stem Cell 14, 673–688 (2014). [PubMed: 24792119]
3. Field AE et al. DNA methylation clocks in aging: categories, causes, and consequences. Mol. Cell 71, 882–895 (2018). [PubMed: 30241605]
4. Zhou W. et al. DNA methylation loss in late-replicating domains is linked to mitotic cell division. Nat. Genet 50, 591–602 (2018). [PubMed: 29610480]
5. Hernando-Herraez I. et al. Ageing affects DNA methylation drift and transcriptional cell-to-cell variability in mouse muscle stem cells. Nat. Commun 10, 4361 (2019). [PubMed: 31554804]
6. Salhab A. et al. A comprehensive analysis of 195 DNA methylomes reveals shared and cell-specific features of partially methylated domains. Genome Biol. 19, 150 (2018). [PubMed: 30266094]
7. Brinkman AB et al. Partially methylated domains are hypervariable in breast cancer and fuel widespread CpG island hypermethylation. Nat. Commun 10, 1749 (2019). [PubMed: 30988298]
8. Janssen A, Colmenares SU & Karpen GH Heterochromatin: guardian of the genome. Annu. Rev. Cell Dev. Biol 34, 265–288 (2018). [PubMed: 30044650]

9. Padeken J, Methot SP & Gasser SM Establishment of H3K9-methylated heterochromatin and its functions in tissue differentiation and maintenance. Nat. Rev. Mol. Cell Biol. 23, 623–640 (2022). [PubMed: 35562425]
10. Allshire RC & Madhani HD Ten principles of heterochromatin formation and function. Nat. Rev. Mol. Cell Biol. 19, 229–244 (2018). [PubMed: 29235574]
11. Wu H. & Zhang Y. Reversing DNA methylation: mechanisms, genomics, and biological functions. Cell 156, 45–68 (2014). [PubMed: 24439369]
12. Li E. & Zhang Y. DNA methylation in mammals. Cold Spring Harb. Perspect. Biol 6, a019133 (2014).
13. Tahiliani M. et al. Conversion of 5-methylcytosine to 5-hydroxymethylcytosine in mammalian DNA by MLL partner TET1. Science 324, 930–935 (2009). [PubMed: 19372391]
14. Okano M, Xie S. & Li E. Cloning and characterization of a family of novel mammalian DNA (cytosine-5) methyltransferases. Nat. Genet 19, 219–220 (1998). [PubMed: 9662389]
15. Genovese G. et al. Clonal hematopoiesis and blood-cancer risk inferred from blood DNA sequence. N. Engl. J. Med 371, 2477–2487 (2014). [PubMed: 25426838]
16. Jaiswal S. et al. Age-related clonal hematopoiesis associated with adverse outcomes. N. Engl. J. Med 371, 2488–2498 (2014). [PubMed: 25426837]
17. Couronne L, Bastard C. & Bernard OA TET2 and DNMT3A mutations in human T-cell lymphoma. N. Engl. J. Med 366, 95–96 (2012). [PubMed: 22216861]
18. Richards EJ & Elgin SC Epigenetic codes for heterochromatin formation and silencing: rounding up the usual suspects. Cell 108, 489–500 (2002). [PubMed: 11909520]
19. Rose NR & Klose RJ Understanding the relationship between DNA methylation and histone lysine methylation. Biochim. Biophys. Acta 1839, 1362–1372 (2014). [PubMed: 24560929]
20. Lopez-Moyado IF et al. Paradoxical association of TET loss of function with genome-wide DNA hypomethylation. Proc. Natl. Acad. Sci. USA 116, 16933–16942 (2019). [PubMed: 31371502]
21. Fang S. et al. Tet inactivation disrupts YY1 binding and long-range chromatin interactions during embryonic heart development. Nat Commun 10, 4297 (2019). [PubMed: 31541101]
22. Li J. et al. Decoding the dynamic DNA methylation and hydroxymethylation landscapes in endodermal lineage intermediates during pancreatic differentiation of hESC.Nucleic Acids Res. 46, 2883–2900 (2018). [PubMed: 29394393]
23. Busch K. et al. Fundamental properties of unperturbed haematopoiesis from stem cells in vivo. Nature 518, 542–546 (2015). [PubMed: 25686605]
24. Izzo F. et al. DNA methylation disruption reshapes the hematopoietic differentiation landscape. Nat. Genet 52, 378–387 (2020). [PubMed: 32203468]
25. Rundberg Nilsson A. et al. Human and murine hematopoietic stem cell aging is associated with functional impairments and intrinsic megakaryocytic/erythroid bias. PLoS One 11, e0158369 (2016).
26. Yan H. et al. Distinct roles for TET family proteins in regulating human erythropoiesis. Blood 129, 2002–2012 (2017). [PubMed: 28167661]
27. Qu X. et al. TET2 deficiency leads to stem cell factor-dependent clonal expansion of dysfunctional erythroid progenitors. Blood 132, 2406–2417 (2018). [PubMed: 30254129]
28. Pang WW et al. Human bone marrow hematopoietic stem cells are increased in frequency and myeloid-biased with age. Proc. Natl. Acad. Sci. USA 108, 20012–20017 (2011). [PubMed: 22123971]
29. Ko M. et al. Ten-Eleven-Translocation 2 (TET2) negatively regulates homeostasis and differentiation of hematopoietic stem cells in mice. Proc. Natl. Acad. Sci. USA 108, 14566–14571 (2011). [PubMed: 21873190]
30. Kowalczyk MS et al. Single-cell RNA-seq reveals changes in cell cycle and differentiation programs upon aging of hematopoietic stem cells. Genome Res. 25, 1860–1872 (2015). [PubMed: 26430063]
31. Kirschner K. et al. Proliferation drives aging-related functional decline in a subpopulation of the hematopoietic stem cell compartment. Cell Rep. 19, 1503–1511 (2017). [PubMed: 28538171]

32. Bergen V. et al. Generalizing RNA velocity to transient cell states through dynamical modeling. Nat. Biotechnol 38, 1408–1414 (2020). [PubMed: 32747759]
33. Pastor WA et al. Genome-wide mapping of 5-hydroxymethylcytosine in embryonic stem cells. Nature 473, 394–397 (2011). [PubMed: 21552279]
34. Huang Y, Pastor WA, Zepeda-Martinez JA & Rao A. The anti-CMS technique for genome-wide mapping of 5-hydroxymethylcytosine. Nat. Protoc 7, 1897–1908 (2012). [PubMed: 23018193]
35. Poleshko A. et al. H3K9me2 orchestrates inheritance of spatial positioning of peripheral heterochromatin through mitosis. Elife 8, e49278 (2019). [PubMed: 31573510]
36. von Meyenn F. et al. Impairment of DNA methylation maintenance is the main cause of global demethylation in naive embryonic stem cells. Mol. Cell 62, 848–861 (2016). [PubMed: 27237052]
37. Challen GA et al. Dnmt3a is essential for hematopoietic stem cell differentiation. Nat. Genet 44, 23–31 (2012).
38. Pappalardi MB et al. Discovery of a first-in-class reversible DNMT1-selective inhibitor with improved tolerability and efficacy in acute myeloid leukemia. Nat. Cancer 2, 1002–1017 (2021). [PubMed: 34790902]
39. Chen Q. et al. GSK-3484862 targets DNMT1 for degradation in cells. NAR. Cancer 5, zcad022 (2023).
40. Hsieh TH et al. Mapping nucleosome resolution chromosome folding in yeast by Micro-C. Cell 162, 108–119 (2015). [PubMed: 26119342]
41. Zhang X. et al. The loss of heterochromatin is associated with multiscale three-dimensional genome reorganization and aberrant transcription during cellular senescence. Genome Res. 31, 1121–1135 (2021). [PubMed: 34140314]
42. Zhang SM et al. KDM5B promotes immune evasion by recruiting SETDB1 to silence retroelements. Nature 598, 682–687 (2021). [PubMed: 34671158]
43. Liu X. et al. Resurrection of endogenous retroviruses during aging reinforces senescence. Cell 186, 287–304 e26 (2023). [PubMed: 36610399]
44. Tsumura A. et al. Maintenance of self-renewal ability of mouse embryonic stem cells in the absence of DNA methyltransferases Dnmt1, Dnmt3a and Dnmt3b. Genes Cells 11, 805–814 (2006). [PubMed: 16824199]
45. Zhang X. et al. DNMT3A and TET2 compete and cooperate to repress lineage-specific transcription factors in hematopoietic stem cells. Nat. Genet 48, 1014–1023 (2016). [PubMed: 27428748]
46. Wilkinson AC et al. Long-term ex vivo haematopoietic-stem-cell expansion allows nonconditioned transplantation. Nature 571, 117–121 (2019). [PubMed: 31142833]
47. Wolf FA, Angerer P. & Theis FJ SCANPY: large-scale single-cell gene expression data analysis. Genome Biol. 19, 15 (2018). [PubMed: 29409532]
48. Xi Y. & Li W. BSMAP: whole genome bisulfite sequence MAPping program. BMC Bioinformatics 10, 232 (2009). [PubMed: 19635165]
49. Zhang Y. et al. Model-based analysis of ChIP-Seq (MACS). Genome Biol. 9, R137 (2008). [PubMed: 18798982]
50. Stark R. & Brown G. DiffBind: differential binding analysis of ChIP-Seq peak data. Cancer Research UK – Cambridge Institute; University of Cambridge (2023).
51. Sun D. et al. MOABS: model based analysis of bisulfite sequencing data. Genome Biol. 15, R38 (2014). [PubMed: 24565500]
52. Poleshko A. et al. Genome-nuclear lamina interactions regulate cardiac stem cell lineage restriction. Cell 171, 573–587 e14 (2017). [PubMed: 29033129]
53. Lund E, Oldenburg AR & Collas P. Enriched domain detector: a program for detection of wide genomic enrichment domains robust against local variations. Nucleic Acids Res. 42, e92 (2014). [PubMed: 24782521]
54. Robinson JT et al. Integrative genomics viewer. Nat. Biotechnol 29, 24–26 (2011). [PubMed: 21221095]
55. Arifin WN & Zahiruddin WM Sample size calculation in animal studies using resource equation approach. Malays. J. Med. Sci 24, 101–105 (2017).

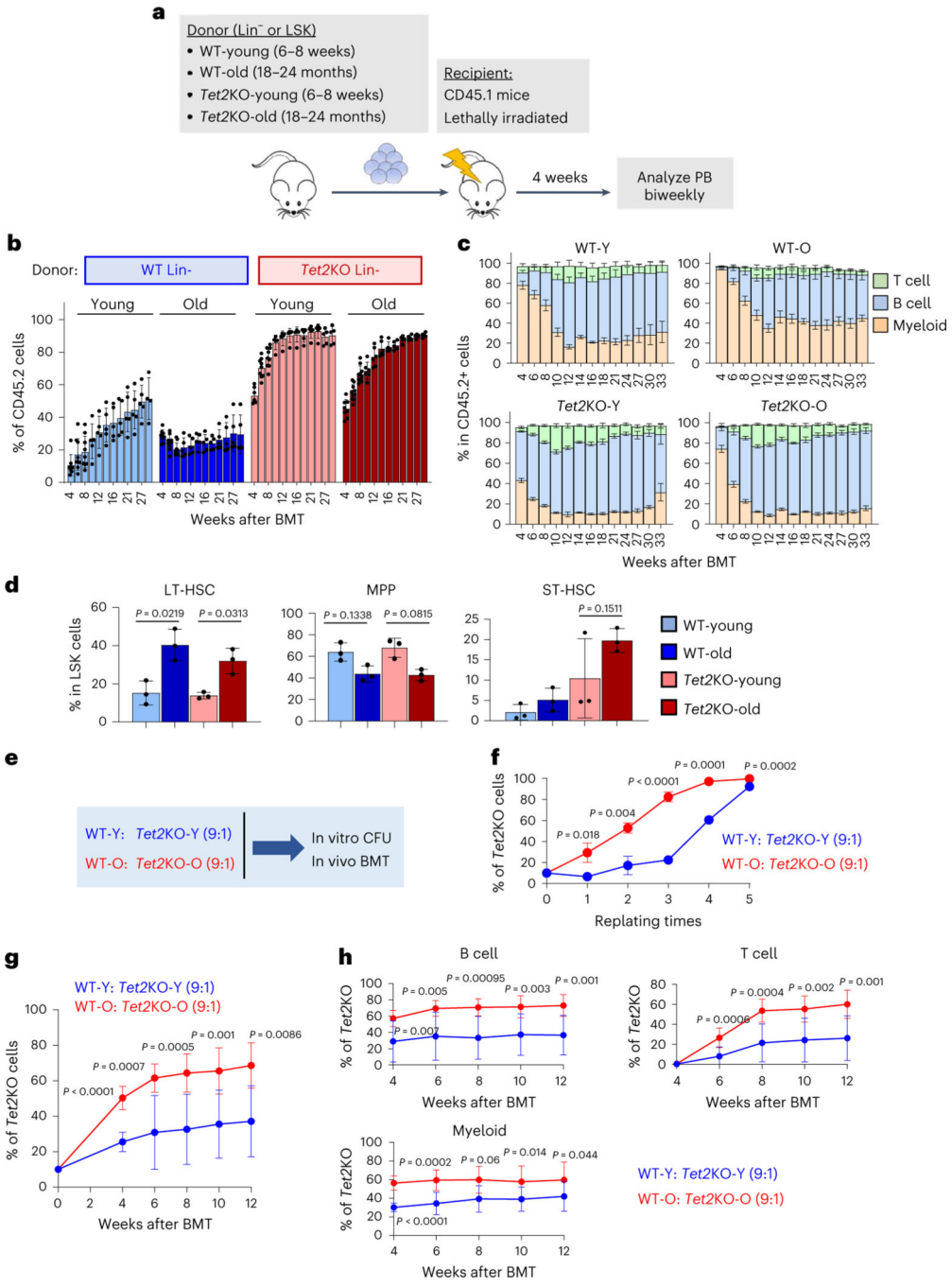

Fig. 1 |. Tet2 depletion rescues age-related decline in HSPC self-renewal and repopulation capability.

a, Experimental setup for the BMT experiments. **b**, Reconstitution efficiency of lethally irradiated CD45.1 mice transferred with Lin$^-$ cells from the indicated donor mice ($n = 2$ female and 3 male donor mice). Measurements were taken biweekly after BMT ($n = 5$–9 recipient mice with equal number of male and female mice per group, each dot represents an individual recipient mouse). Data are shown as mean ± s.d.; *P* values are listed in Supplementary Table 1 (two-way analysis of variance (ANOVA) test). **c**, Lineage analysis of

peripheral blood collected from CD45.1 recipient mice (n = 5–9/group). Each dot represents an individual recipient mouse. Data are presented as mean ± s.d. (two-way ANOVA test; see exact P values in Supplementary Table 1). **d**, Percentage of LT-HSC, MPP, and ST-HSC in LSK cells isolated from bone marrow of CD45.1 recipient mice (12 weeks after BMT). Data are shown as mean ± s.d.; n = 3 (2 male and 1 female) mice (two-way ANOVA multiple comparison post hoc test, Supplementary Table 1). **e**, Experimental design for in vitro and in vivo competition assays. **f**, In vitro serial CFU assay. The percentage of cells derived from *Tet2*KO cells was measured at the indicated replating time points. Data are shown as mean ± s.d.; n = 3 independent experiments (repeated-measures ANOVA test, Supplementary Table 1). **g**, In vivo competition experiments were carried out by transplanting WT and *Tet2*KO HSPCs (9:1 ratio) into lethally irradiated CD45.1 recipient mice (n = 3 donors, 2 male and 1 female donor mice). The percentage of cells derived from *Tet2*KO HSPCs was measured in the peripheral blood biweekly. Data are shown as mean ± s.d.; n = 9 (5 male and 4 female) recipient mice per group (repeated-measures ANOVA test, Supplementary Table 1). **h**, Percentage of cells derived from the *Tet2*KO groups in the peripheral blood of the recipient mice from Fig. 1e. Data are shown as mean ± s.d.; n = 9 recipient mice per group repeated-measures ANOVA test, Supplementary Table 1).

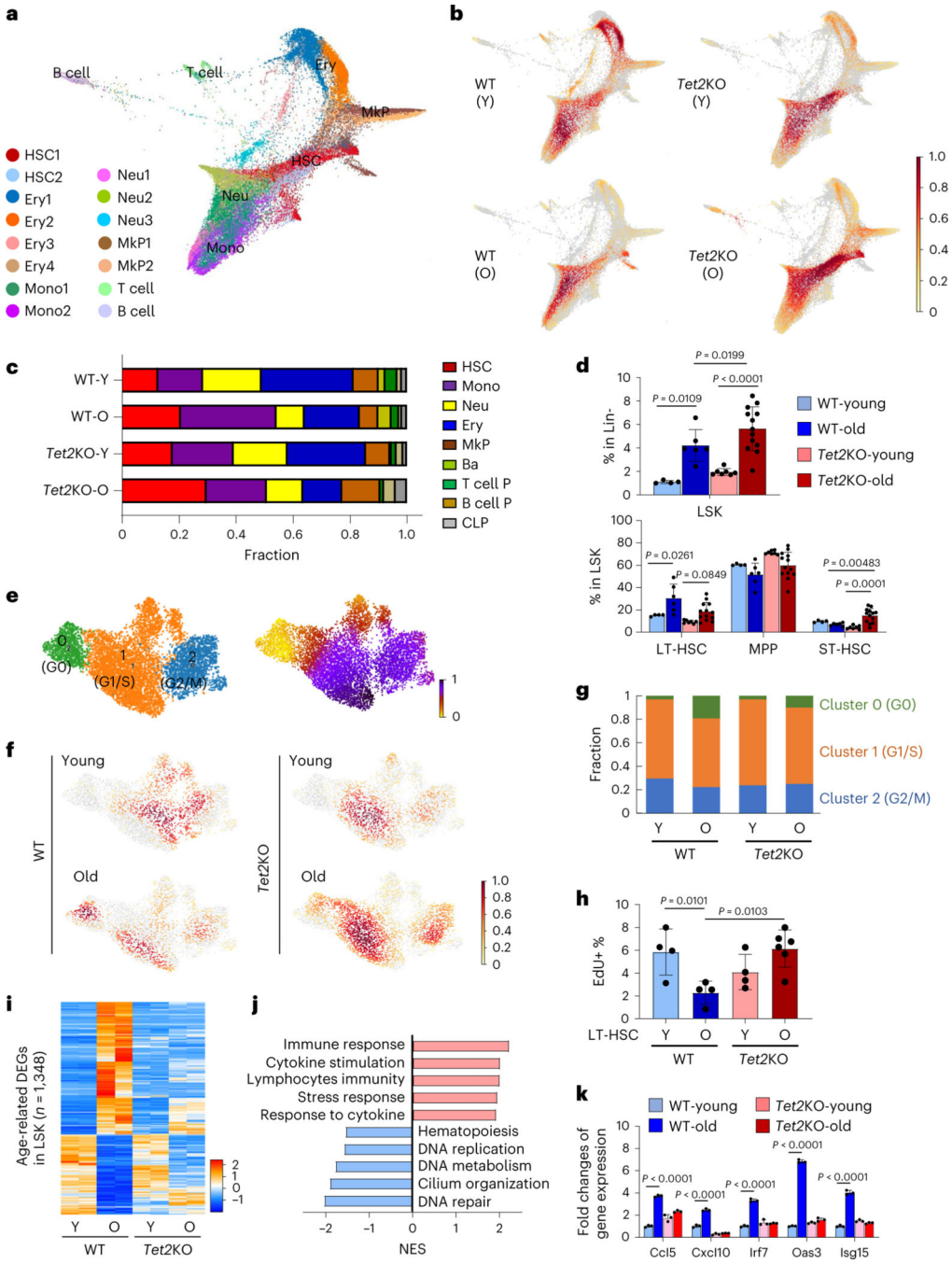

Fig. 2 |. Distinct transcriptional alterations during WT and *Tet2*KO HSPCs aging.

a, UMAP dimensionality reduction of all analyzed Lin$^-$ cells (n = 31,399) (WT-young, 8,276; WT-old, 6,249; *Tet2*KO-young, 5,479; *Tet2*KO-old, 11,395). HSC, hematopoietic stem cells; Mono, monocyte progenitor; Neu, neutrophil/granulocyte progenitor; Ery, erythroid progenitor; MkP, megakaryocyte progenitor. **b**, UMAP plots showing cell densities during aging in specified groups. Red color, high cell density in the corresponding group. Y, young; O, old. **c**, The fraction of each cell cluster within the designated groups. **d**, Flow cytometry analysis showing the percentage of LT-HSC, MPP and ST-HSC populations

in LSK ($Lin^{-}cKit^{+}Sca1^{+}$) cells purified from bone marrow of gender- and aged-matched congenic mice (WT-young, WT-old, *Tet2*KO-young, and *Tet2*KO-old). Data are shown as mean ± s.d.; n = 4–13 (equal number of male and female mice) per group. Each dot represents an individual recipient mouse (two-way ANOVA multiple comparison post hoc test, Supplementary Table 1). **e**, Pseudotime analysis (right) revealing the differentiation process projected in the UMAP-based embedding (left) within the HSC population at different cell cycles (n = 7,222). Yellow, inferred earlier stage; purple, inferred later stage. **f**, Density plots showing HSC densities in WT or *Tet2*KO groups during aging. **g**, Quantification of the fraction of cells at each cell cycle stage (G0, G1/S, and G2/M). **h**, The percentage of EdU-positive cells in LT-HSCs purified from the indicated groups. Data are shown as mean ± s.d.; n = 4–6 mice (equal number of male and female mice) per group with each dot represents an individual mouse (two-way ANOVA multiple comparison post hoc test, Supplementary Table 1). **i**, Heatmap illustrating aging-related DEGs in HSPCs purified from the indicated groups. Age-related DEGs were identified by comparing the bulk RNA-seq data between WT-young and WT-old HSPCs. **j**, Gene set enrichment analysis on the age-related DEGs shown in Fig. 2i and Supplementary Table 2. **k**, Real-time qPCR validation on the expression of age-related DEGs involved in innate immunity in LSK cells sourced from the indicated groups. Data are shown as mean ± s.d.; n = 3 independent experiments; one-way ANOVA analysis (see exact P values in Supplementary Table 1).

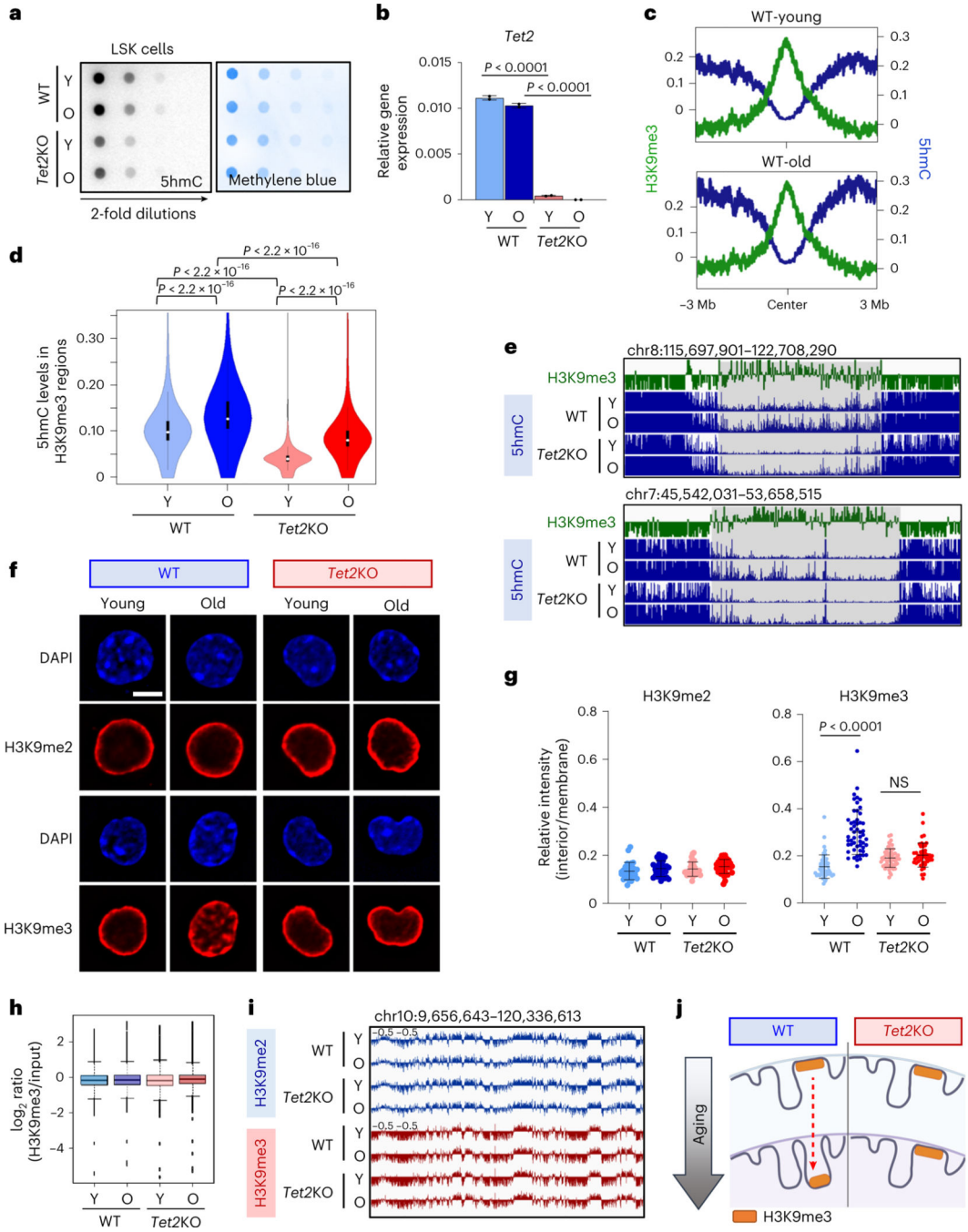

Fig. 3 |. Tet2 loss prevents the spatial relocalization of H3K9me3-marked genomic regions from the nuclear periphery to the nucleoplasm during HSPC aging.

a, Dot-blot analysis showing the global 5hmC level in LSK cells from the indicated mice. Methylene blue staining was used to ensure equal loading. **b**, Real-time qPCR analysis showing *Tet2* expression in LSK cells purified from the indicated groups. Data are shown as mean ± s.d.; $n = 3$ independent experiments (two-way ANOVA multiple comparison post hoc test, Supplementary Table 1). **c**, Curve plot displaying the mean 5hmC signals (blue) within H3K9me3-marked regions (green) in LSK cells purified from

WT-Young (top) or WT-Old (bottom) mice. **d**, Violin plot illustrating 5hmC enrichment within H3K9me3-marked heterochromatin in LSK cells purified from the indicated mice. (two-sided Kolmogorov-Smirnov test), $n = 2$ biological replicates. **e**, Genome browser views presenting the 5hmC level (blue, CMS-IP-seq; scale: 0 to 1.1) within H3K9me3-marked heterochromatins in LSK cells from the indicated groups. **f**,**g**, Representative images (**f**) and quantification (**g**) of IF staining intensities for H3K9me2 and H3K9me3 in LSK cells purified from WT-young, WT-old, *Tet2*KO-young and *Tet2*KO-old mice. DAPI was used to stain the whole nuclei. Scale bar, 5 μm. Data are shown as mean ± s.d.; $n = 48–53$ cells ($n = 5$, 3 male and 2 female donor mice) (two-tailed Student's *t*-test). NS, not statistically significant. **h**, Boxplot showing the H3K9me3 enrichment (log2 ratio against the input) in LSK cells purified from WT-young, WT-old, *Tet2*KO-young and *Tet2*KO-old mice. $n = 2$ biological replicates. **i**, The genome browser view of H3K9me2 (blue) and H3K9me3 (red) distributions in LSK cells purified from WT-young (Y), WT-old (O), *Tet2*KO-young, and *Tet2*KO-old mice. **j**, Schematic illustration of the spatial relocalization, but not changes in genomic binding of H3K9me3 in WT HSPCs during aging. This age-related scenario was not evident in the *Tet2*KO group.

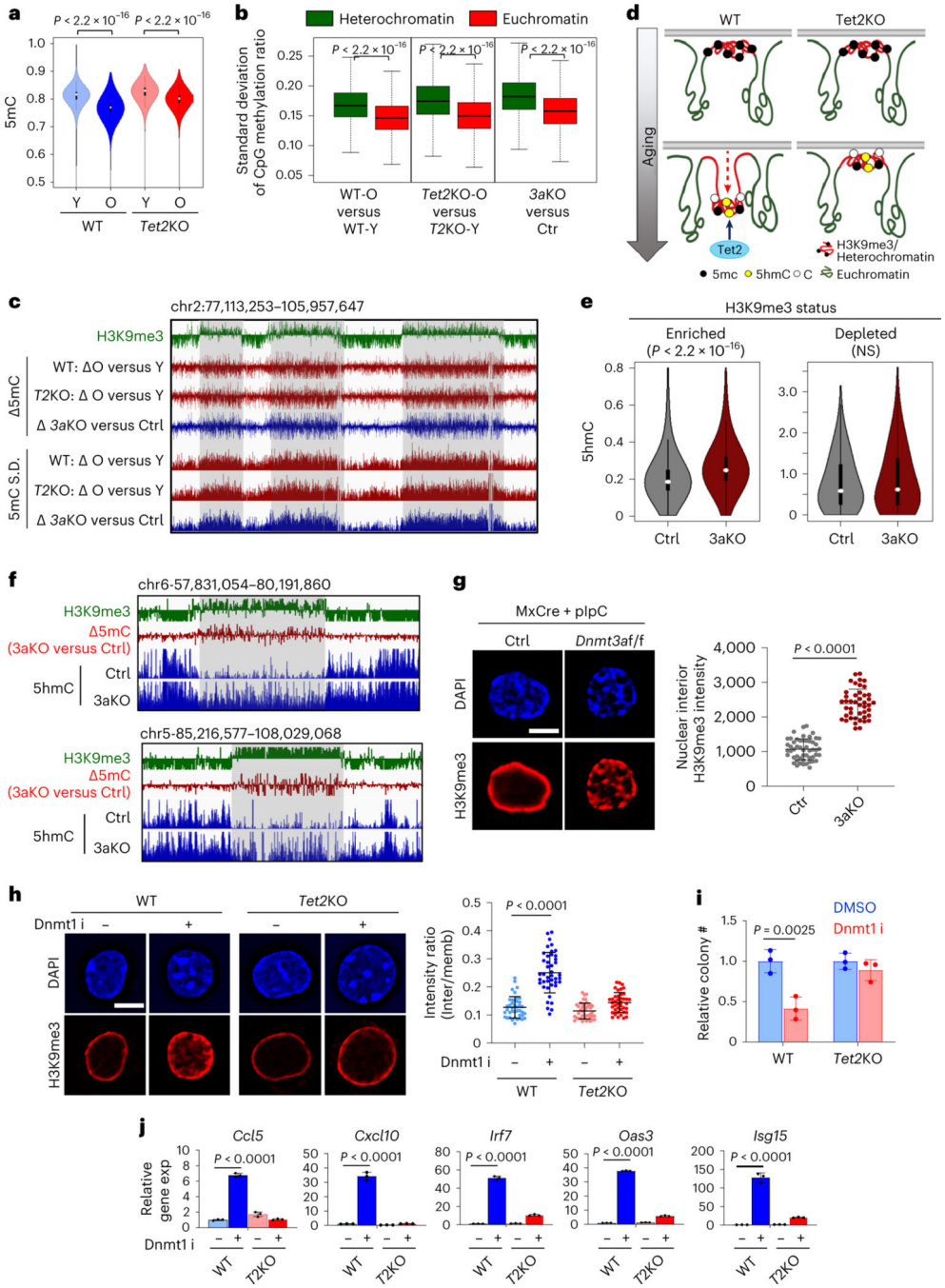

Fig. 4 |. DNA methylation dysregulation contributes to the spatial relocalization of H3K9me3 in HSPCs.

a, Violin plot displaying the 5mC level within heterochromatins in LSK cells (two-sided Kolmogorov-Smirnov test). **b**, Boxplot illustrating the standard deviation of DNA methylation difference at each CpG site between the indicated comparison groups in 10-kb bins in heterochromatin (green) or euchromatin (red) based on H3K9me3 enrichment (two-sided Kolmogorov-Smirnov test). **c**, Genome browser views. Δ5mC: DNA methylation difference at each CpG sites (scale: −0.2 to 0.2). 5mC S.D.: standard deviation of

DNA methylation changes (scale: 0.1–0.3). O, old; Y, young; T2KO, *Tet2*KO; 3aKO, *Dnmt3a*KO; Ctrl, control. The H3K9me3 track (scale: −0.5 to 0.5) represents WT-Y LSK cells. **d**, A proposed working model. **e**, Violin plot illustrating 5hmC enrichment within heterochromatin and euchromatin in LSK cells from the indicated mice treated with pIpC. N.S.: no statistical significance. $n = 2$ biological replicates (two-sided Kolmogorov-Smirnov test). **f**, Genome browser views of 5hmC (blue, scale: 0–2.5) in LSK cells. Δ5mC (red, scale: −0.2 to 0.2). H3K9me3 (green, scale: −0.5 to 0.5) was derived from WT-Y LSK cells. **g**, IF staining of H3K9me3 in LSK cells from the indicated mice 4 weeks after pIpC treatment. Scale bar, 5 μm. Data are shown as mean ± s.d.; $n = 50$ cells per group (from 5 mice) (two-tailed Student's *t*-test). **h**, IF staining of H3K9me3 in young WT and *Tet2*KO LSK cells after 10-day treatment of DMSO or a Dnmt1 inhibitor (Dnmt1i). Scale bar, 5 μm. Data are shown as mean ± s.d.; $n = 45$ cells per group (from 3 male and 2 female mice) (two-way ANOVA multiple comparison post hoc test, Supplementary Table 1). **i**, CFU assay of young WT and *Tet2*KO LSK cells treated with DMSO or Dnmt1i. Data are shown as mean ± s.d.; $n = 3$ independent experiments (two-way ANOVA multiple comparison post hoc test, Supplementary Table 1). **j**, Real-time quantitative PCR (RT-qPCR) analysis of age-related DEGs tied to innate immunity in young WT and *Tet2*KO LSK cells treated with DMSO or Dnmt1i. exp, expression. Data are shown as mean ± s.d.; $n = 3$ independent experiments (one-way ANOVA analysis; see exact *P* values in Supplementary Table 1).

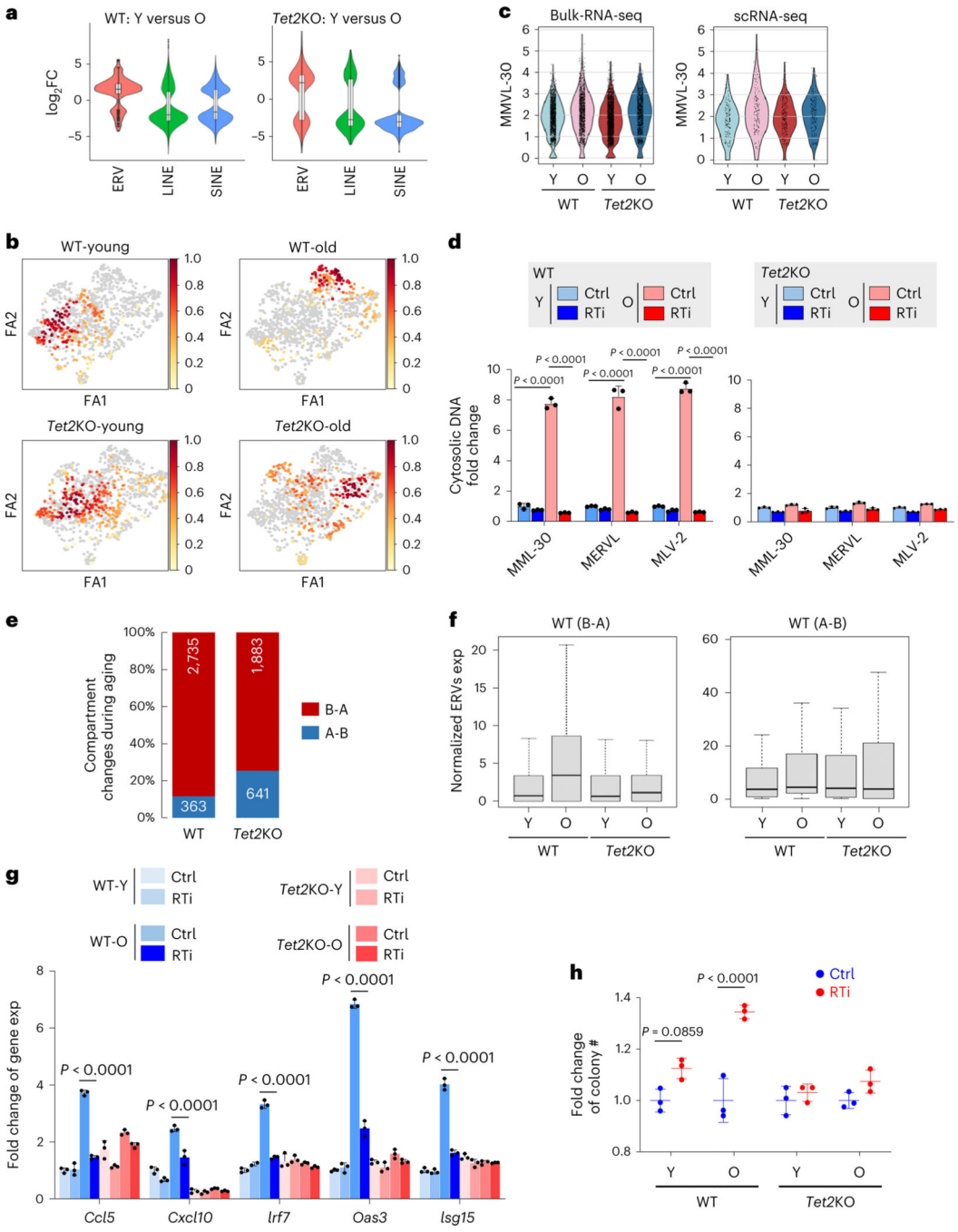

Fig. 5 |. Upregulation of repetitive elements in aged HSPCs contributes to their functional decline.

a, Violin plot displaying age-related (young versus old) differential expression of repetitive elements in WT (left) and *Tet2*KO (right) groups. $n = 2$ biological replicates. **b**, Density plots showing HSCs identified based on the expression of repetitive elements. **c**, Violin plot showing the distribution of normalized expression levels of *MMVL-30* from bulk RNA-seq in LSK cells (left) or the identified HSCs in scRNA-seq (right) from the indicated groups. **d**, RT-PCR analysis of cytosolic DNA derived from the indicated ERVs in young

(blue) or old (red) WT (left) and *Tet2*KO (right) HSPCs treated with either DMSO or an RTi. Data are shown as mean ± s.d.; $n = 3$ independent experiments; one-way ANOVA analysis (Supplementary Table 1). $n = 2$ biological replicates. **e**, The percentage of compartments undergoing age-related (young versus old) changes in WT or *Tet2*KO HSPCs. The number of compartments in each category is listed. Red, compartment with B-to-A change; Blue, Compartment with A-to-B change. **f**, Normalized expression of ERVs derived from H3K9me3-marked genomic regions with age-related compartment changes (B-to-A or A-to-B). $n = 2$ biological replicates. **g**, RT-PCR analysis of age-related DEGs involved in innate immunity in HSPCs obtained from the indicated groups treated with either DMSO or RTi. Data are shown as mean ± s.d. ($n = 3$ independent experiments); one-way ANOVA analysis (Supplementary Table 1). **h**, CFU assay conducted on HSPCs purified from the indicated groups treated with DMSO or RTi. Data are shown as mean ± s.d. ($n = 3$ independent experiments) (one-way ANOVA analysis; see exact *P* values in Supplementary Table 1).